Adeno-associated virus type 2 (AAV2) uncoating is a stepwise process and is linked to structural reorganization of the nucleolus (full title)

AAV2 uncoating occurs stepwise and depends on nucleolar reorganization (short title)

Sereina O. Sutter[1¶], Anouk Lkharrazi[1¶], Elisabeth M. Schraner[1], Kevin Michaelsen[1], Anita Felicitas Meier[1], Bernd Vogt[1], Hildegard Büning[2], and Cornel Fraefel[1*]

[1] Institute of Virology, University of Zurich, Zurich, Switzerland

[2] Institute of Experimental Hematology, Hannover Medical School, Hannover, Germany

[*] Corresponding author

E-mail: cornel.fraefel@uzh.ch (CF)

[¶] These authors contributed equally to this work.

Abstract

Nucleoli are membrane-less structures located within the nucleus and are known to be involved in many cellular functions, including stress response and cell cycle regulation. Besides, many viruses can employ the nucleolus or nucleolar proteins to promote different steps of their life cycle such as replication, transcription and assembly. While adeno-associated virus type 2 (AAV2) capsids have previously been reported to enter the host cell nucleus and accumulate in the nucleolus, both the role of the nucleolus in AAV2 infection, and the viral uncoating mechanism remain elusive. In all prior studies on AAV uncoating, viral capsids and viral genomes were not directly correlated on the single cell level, at least not in absence of a helper virus. To elucidate the properties of the nucleolus during AAV2 infection and to assess viral uncoating on a single cell level, we combined immunofluorescence analysis for detection of intact AAV2 capsids and capsid proteins with fluorescence *in situ* hybridization for detection of AAV2 genomes. The results of our experiments provide evidence that uncoating of AAV2 particles occurs in a stepwise process that is completed in the nucleolus and supported by alteration of the nucleolar structure.

Author Summary

Adeno-associated virus (AAV) capsids have been reported to enter the host cell nucleus and accumulate in the nucleolus. However, both the role of the nucleolus in AAV2 infection as well as the viral uncoating mechanism remain unknown. Here, we provide evidence that uncoating of the AAV2 particle is a stepwise process that is completed in the nucleolus and supported by alteration of the nucleolar morphology.

Introduction

Adeno-associated virus type 2 (AAV2) is a small, non-pathogenic, helper virus-dependent parvovirus with a single-stranded (ss) DNA genome of approximately 4.7 kb. In absence of a helper virus, AAV2 can integrate its genome site-preferentially into the adeno-associated virus integration site (AAVS1) on human chromosome 19 or persist in an episomal form in the nucleus [1,2]. Co-infection with a helper virus, such as herpes simplex virus type 1 (HSV-1), leads to a lytic replication cycle including the production of progeny virus particles [3]. The AAV2 genome consists of two large open reading frames (ORFs) flanked by 145 nt long inverted terminal repeats (ITRs) located on either side. The *rep* gene encodes the four non-structural Rep proteins, two of which are transcribed from the p5 and the p19 promoter, respectively. An alternative splice site regulates expression of the alternative transcripts, whereby the unspliced RNAs encode Rep78 and Rep52, whereas Rep68 and Rep40 are encoded by their corresponding spliced variant [4,5]. The promoter activity is regulated by the Rep binding site (RBS), therefore allowing the Rep protein to act either as a trans-activator or repressor [6]. In the absence of a helper virus, only little expression of Rep takes place, which nonetheless is sufficient to repress any further transcription.

The three structural proteins VP1, VP2 and VP3, constituting the icosahedral capsid, are encoded by the *cap* gene. Furthermore, the *cap* gene encodes the assembly-activating protein (AAP) and the membrane-associated accessory protein (MAAP) by means of nested alternative ORFs [7,8].

Adeno-associated viruses exhibit a broad cellular tropism [9]. Referring to AAV2, the cellular receptors facilitating cell attachment and entry, include heparan sulfate proteoglycan, human fibroblast growth factor receptor 1, $\alpha_V\beta_5$ integrin, $\alpha_5\beta_1$ integrin (reviewed in [10]) and the host factor KIAA0319L (synonymous AAVR) [11]. Different

entry pathways were proposed for AAV2, including clathrin- and dynamin-dependent endocytosis or internalization supported by the Ras-related C3 botulinum toxin substrate 1 (Rac1), a small GTPase and a major effector of macropinocytosis (reviewed in [10]). However, internalization through clathrin-independent carriers (CLICs) and GPI-enriched endocytic compartments (GEECs) was suggested to be part of the major endocytic infection route [12]. It was shown that acidification in endocytic compartments and the activity of proteases trigger conformational changes of the AAV2 capsid, leading to the exposure of the N-terminal domain of the VP1 protein, known as VP1 unique region ($VP1_u$). $VP1_u$ containing a phospholipase A2 domain (PLA_2) as well as a nuclear localization signal enables the endosomal escape of AAV2 and nuclear entry [13]. After nuclear entry, AAV2 capsids were shown to accumulate in nucleoli mediated by nucleolar associated proteins [14,15]. Nucleoli are membrane-less structures located within the nucleus and are organized in three distinct compartments. The fibrillary center is surrounded by the dense fibrillary compartment and further embedded in the granular compartment. The structural (re-)organization of the nucleolus is strongly linked to its function in transcription and pre-rRNA processing. Besides, the nucleolus is known to be involved in many other cellular functions, including stress response, cell cycle regulation and apoptosis (reviewed in [16–19]). Additionally, many different viruses such as HSV-1, human immunodeficiency virus type 1 (HIV-1) or adenovirus (AdV) can harness the nucleolus or specific nucleolar proteins in order to promote different steps of their life cycle including replication, transcription and assembly [20,21]. While AAV2 capsids have previously been reported to enter the host cell nucleus and accumulate in the nucleolus in a nucleolin- and nucleophosmin-dependent manner [14,15], both the role of the nucleolus in AAV2 infection, and the viral uncoating mechanism remain elusive. The current paradigm proposes a model where AAV2

capsids accumulate in the nucleolus upon nuclear entry and then translocate to the nucleoplasm for uncoating [22]. This model is based on the observation that treating cells with either proteasome inhibitors or hydroxyurea, both known to enhance AAV2 transduction, improve nucleolar accumulation and mobilization of virions into the nucleoplasm, respectively. Besides, the post-transcriptional silencing of nucleophosmin, a highly expressed multifunctional nucleolar phosphoprotein, enhanced nucleolar accumulation and increased transduction similar to the treatment with proteasome inhibitors, while silencing of nucleolin, an abundant non-ribosomal protein of the nucleolus [23], mobilized capsids to the nucleoplasm and enhanced transduction similar to the treatment with hydroxyurea. Other studies concluded that uncoating occurs before or during nuclear entry [24–26]. These conclusions were mainly based on the fact that only AAV2 genomes were detected in the nucleus and that perinuclear genomes did not always co-localize with AAV2 capsids. In all these prior studies on AAV uncoating, however, viral capsids and viral genomes were not directly correlated on the single cell level, at least not in absence of a helper virus [27], but rather quantified by quantitative (q)PCR, Western or slot blot analysis, single AAV capsid specific immunostainings or fluorescently labelled AAV virions [22,24,26–31].

To elucidate the sink-like properties of the nucleolus during AAV2 infection and to assess viral uncoating on a single cell level, we combined immunofluorescence (IF) analysis to detect intact AAV2 capsids as well as capsid proteins with fluorescence *in situ* hybridization (FISH) to visualize AAV2 genomes. The results of our experiments support the hypothesis that AAV2 uncoating takes place in the nucleolus in a cell cycle-dependent manner.

Results

AAV2 capsids and AAV2 genomes accumulate in the nucleoli of infected cells

Previous studies have shown that nucleoli act as a sink for incoming AAV2 capsids. However, it is not known whether the nucleolar localization is merely a result of the interaction of the AAV2 capsids with specific nucleolar proteins or a pre-requisite for an early step of the viral replication cycle such as uncoating or second strand-synthesis. While prior reports suggested that AAV2 capsids translocate from the nucleoli to the nucleoplasm for uncoating, these studies have not simultaneously tracked capsids and genomes on the single cell level [22,32].

Here, we investigated the spatial and temporal distribution of both AAV2 capsids and AAV2 genomes in single cells. For this, normal human fibroblast (NHF) cells were either mock-infected or infected with wild-type (wt) AAV2 at a multiplicity of infection (MOI) of 20’000 genome containing particles (gcp) per cell (herein referred to as MOI). The cells were fixed at different time points post infection and processed for combined multicolor immunofluorescence (IF) analysis to detect AAV2 particles using an antibody that detects a conformational capsid epitope and fluorescence *in situ* hybridization (FISH) to detect AAV2 genomes (hereinafter referred to as IF-FISH). The results showed both AAV2 capsids and AAV2 DNA accumulated in the nucleoli of wtAAV2 infected cells over time (Fig 1, A and B). Neither AAV2 capsids nor genomes were detected in the nucleoli upon infection of cells with mutant AAV2 ^{76}HD/AN (S1 Fig) which contains two mutated residues in the catalytic center of the phospholipase A2 (PLA_2) domain and is therefore deficient for endosomal escape [33].

Interestingly, we did not only observe capsid-positive, genome-negative (AAV2 capsid+DNA-) signals in the cytoplasm, as it would be expected when capsids are intact and therefore do not allow binding of the FISH probe to the virus genome, but frequently also capsid-positive, genome-positive signals (AAV2 capsid+DNA+; see insets Fig 1A, 0 h, 3 h, 10 h). This indicates that either the virus stocks contained improperly encapsidated AAV2 DNA or that the AAV2 genome is accessible to the FISH probe within the cytoplasm (herein referred to as genome accessibility). While the main focus of this study was on simultaneously tracking AAV2 capsids and AAV2 genomes in the nucleus, it was important to first investigate the origin of the AAV2 capsid-positive and AAV2 genome-positive signals in the cytoplasm.

Fig 1. Spatial distribution of AAV2 capsids and DNA over time. NHF cells were infected with wtAAV2 (MOI 20`000). At various time points post infection, the cells were fixed and processed for multicolor IF analysis combined with FISH and confocal laser scanning microscopy (CLSM). Nucleoli (Nuc) were visualized using an antibody against fibrillarin (yellow). Intact capsids were stained using an antibody that detects a conformational capsid epitope (green). AAV2 DNA (magenta) was detected with an Alexa Fluor (AF) 647 labeled, amine-modified DNA probe that binds to the AAV2 genome. (A) Spatial and temporal distribution of AAV2 capsids and DNA. The white line represents the edge of the nucleoli (fibrillarin staining). (B) Orthogonal projections of a z-stack at 24 hpi. The white line represents the edge of the nucleus (4`,6-diamidino-2-phenylindole (DAPI) staining). (C) Image-based quantification of the uncoating rate of 50 individual cells per time point in the nucleolus and (D) in the cytoplasm. p-values were calculated using an unpaired Student`s t-test (* - $p \leq 0.05$, ** - $p \leq 0.01$, *** - $p \leq 0.001$, **** - $p \leq 0.0001$).

Co-detection of AAV2 capsids and AAV2 genomes in the cytoplasm is supported by AAV2 genome accessibility and requires acidification

To address the question whether wtAAV2 stocks contained improperly encapsidated AAV2 genomes, wtAAV2 particles were directly applied to fibronectin coated coverslips and processed for IF-FISH (Fig 2A). While in the untreated wtAAV2 samples all capsid-positive signals (green) were genome-negative, only genome-positive signals (red) but no capsids were observed upon incubation for 5 min at 75˚C, which is known to destabilize AAV2 capsids [34]. In the heat-treated samples, the AAV2 capsids were indeed disintegrated as confirmed by electron microscopy (Fig 2B), and the AAV2 genome signals disappeared upon DNase I treatment (Fig 2A). These experiments demonstrate that the virus stocks were not contaminated with improperly encapsidated AAV2 DNA. To address the hypothesis that co-detection of AAV2 capsids and AAV2 genomes in the cytoplasm is enabled by genome accessibility, we determined the ratios of AAV2 capsid+DNA+/AAV2 capsid+DNA- signals at different timepoints after infection using CellProfiler. As shown in Fig 1C and 1D, these ratios significantly increased with time of infection, both in the cytoplasm and the nucleoli, indicating AAV2 capsid+DNA- signals decrease over time.

As acidification has been shown to lead to conformational changes in the AAV2 capsid and to be important for AAV2 infection, endosomal escape and nuclear entry in particular [25], we examined whether acidification leads to co-detection of AAV2 capsid- and AAV2 genome signals in the cytoplasm. To this end, NHF cells were treated with bafilomycine A1 (50 or 200 nM) 1 h prior to infection with wtAAV2 (MOI 20`000). At 3 hours post infection (hpi), the samples were processed for IF-FISH and

CLSM. Treating cells with bafilomycine A1, a vacuolar H+-ATPase inhibitor which blocks endosomal acidification, significantly reduced the import of AAV2 capsids into the nucleus (Fig 3C), as demonstrated previously [25], and also the AAV2 capsid+DNA+/AAV2 capsid+DNA- signal ratios in the cytoplasm (Fig 3, A and B; see also insets in Fig 3A). Collectively, these experiments confirm the specificity of the IF-FISH assay and support the hypothesis that the co-localization of AAV2 capsids and AAV2 DNA in the cytoplasm is due to genome accessibility and is enhanced by acidification.

Fig 2. AAV2 particles on fibronectin coated coverslips. (A) wtAAV2 particles were directly applied to fibronectin coated coverslips and processed for IF analysis combined with FISH and CLSM. Intact capsids were stained using an antibody that detects a conformational capsid epitope (green). AAV2 DNA (red) was detected with an Alexa Fluor (AF) 647 labeled, amine-modified DNA probe that binds to the AAV2 genome. (B) Electron photomicrographs show complete disintegration of the AAV2 capsids at 75°C.

Fig 3. Acidification enhances genome accessibility of AAV2. NHF cells were treated with bafilomycine A1 (50 or 200 nM) or DMSO 1 h prior to infection with wtAAV2 (MOI 20`000). At 3 hpi, the cells were fixed and processed for multicolor IF analysis combined with FISH and CLSM. Nucleoli (Nuc) were visualized using an antibody against fibrillarin (yellow). Intact capsids were stained using an antibody that detects a conformational capsid epitope (green). AAV2 DNA (magenta) was detected with an Alexa Fluor (AF) 647 labeled, amine-modified DNA probe that binds to the AAV2 genome. (A) Genome accessibility of AAV2 capsids after inhibition of the endosome-lysosome system acidification. The white line represents

the edge of the nucleoli (fibrillarin staining). (B) Image-based quantification of the genome accessibility (ratio of AAV2 capsid+DNA+/AAV2 capsid+DNA- signal) of 50 individual cells per sample in the cytoplasm and (C) nuclear AAV2 capsid counts. p-values were calculated using an unpaired Student`s t-test (* - $p \leq 0.05$, ** - $p \leq 0.01$, *** - $p \leq 0.001$, **** - $p \leq 0.0001$).

Detection of AAV2 capsids negatively correlates with detection of AAV2 capsid proteins

After establishing that the co-detection of AAV2 capsids and AAV2 genomes by combined IF-FISH and CLSM is not because of improperly encapsidated virus particles, we continued to analyze the distribution of AAV2 capsids and genomes in the nuclei of individual cells. For this, NHF cells were mock-infected or infected with wtAAV2 (MOI 20`000) and 24 h later processed for combined IF-FISH and CLSM to detect AAV2 capsids and genomes. Interestingly, we observed three distinct patterns of nucleolar AAV2 genome and AAV2 capsid staining: (I) nucleoli with robust AAV2 genome and AAV2 capsid signal, (II) nucleoli with robust AAV2 DNA signal but weak AAV2 capsid signal, and (III) nucleoli in which only the viral DNA was detected in absence of capsids (Fig 4, A and B, see also S1 movie). The pattern, in particular the observation of AAV2 DNA in the nucleoli in absence of AAV2 capsids, led us to the hypothesis that complete AAV2 uncoating takes place in the nucleolus.

If the absence of AAV2 capsid staining in the nucleoli with positive AAV2 genome signal was indeed due to complete viral uncoating, we would expect the presence of disassembled AAV2 capsid proteins in those nucleoli. To assess this hypothesis, NHF cells were mock-infected or infected with wtAAV2 (MOI 20`000) and 24 h later

processed for combined IF-FISH and CLSM to detect AAV2 capsids (conformational epitope), AAV2 capsid proteins (linear epitope) and AAV2 DNA (Fig 5, S2 Fig and Fig 9). The results show a negative correlation of AAV2 capsids and AAV2 capsid proteins in the nucleolus, supporting the hypothesis that AAV2 uncoating indeed takes place in the nucleoli. For technical reasons, co-staining of AAV2 capsids, AAV2 capsid proteins VP1/2/3 and AAV2 DNA did not allow to directly visualize nucleoli. However, the DAPI staining in Fig 5 indirectly reveals the position of the nucleoli. Moreover, individual staining of either AAV2 capsids or AAV2 capsid proteins together with AAV2 DNA and a nucleolar marker demonstrated that both intact AAV2 capsids (e.g., Fig 1) and AAV2 capsid proteins VP1/2 (Fig 5B) accumulated with AAV2 DNA in nucleoli.

Intriguingly, we noticed a distinct difference in the nucleolar structure when comparing AAV2 DNA-positive nucleoli that were positive also for intact AAV2 capsids with AAV2 DNA-positive nucleoli that were negative for intact AAV2 capsids or positive for AAV2 capsid proteins. Specifically, the nucleoli appeared dense when positive for both AAV2 DNA and AAV2 capsids and dispersed when positive for AAV2 DNA and negative for AAV2 capsids or positive for AAV2 DNA and AAV2 capsid proteins (Fig 4A, Fig 5B). Image-based quantification of the mean integrated intensity of AAV2 capsid signals relative to the nucleolar structure revealed a higher capsid signal intensity in dense nucleoli than in dispersed nucleoli (Fig 4C). Overall, these experiments imply that complete AAV2 uncoating takes place in the nucleoli and coincides with changes in the nucleolar structure.

As the ratios of dense to dispersed nucleoli was comparable in mock-infected and wtAAV2 infected cells (S3 Fig), we hypothesized that not virus infection *per se* but cellular processes such as apoptosis, stress response, or cell cycle regulation are responsible for the different structures of AAV2 capsid-positive and AAV2 DNA-

274 positive versus AAV2 capsid-negative and AAV2 DNA-positive nucleoli and may
275 thereby control AAV2 uncoating.
276
277 **Fig 4. Absence of intact AAV2 capsids in AAV2 genome positive nucleoli**
278 **points towards complete viral uncoating.** NHF cells were infected with wtAAV2
279 (MOI 20`000). At 24 hpi, the cells were fixed and processed for multicolor IF analysis
280 combined with FISH and CLSM. Nucleoli (Nuc) were visualized using an antibody
281 against fibrillarin (yellow). Intact capsids were stained using an antibody that detects
282 a conformational capsid epitope (green). AAV2 DNA (magenta) was detected with an
283 Alexa Fluor (AF) 647 labeled, amine-modified DNA probe that binds to the AAV2
284 genome. Nuclei were counterstained with DAPI and illustrated as white lines. (A)
285 Distinct pattern (I - III) of AAV2 capsid signal in cells with AAV2 genome positive
286 nucleoli. (B) Quantification of 50 individual cells with distinct AAV2 capsid signal. (C)
287 Image-based quantification of the integrated intensity of AAV2 capsid signals in
288 dense or dispersed nucleoli of 70 individual cells. p-values were calculated using an
289 unpaired Student`s t-test (* - $p \leq 0.05$, ** - $p \leq 0.01$, *** - $p \leq 0.001$, **** - $p \leq 0.0001$).
290
291 **Fig 5. Co-detection of AAV2 DNA with AAV2 capsids and AAV2 capsid**
292 **proteins.** NHF cells were infected with wtAAV2 (MOI 20`000). At 24 hpi, the cells
293 were fixed and processed for multicolor IF analysis combined with FISH and CLSM.
294 (A) Intact capsids (green) or capsid proteins (yellow) were detected using either an
295 antibody against intact AAV2 capsids (conformational capsid epitope) or an
296 antibody (linear epitope) against VP1, VP2 and VP3. AAV2 DNA (red) was detected
297 with an Alexa Fluor (AF) 647 labeled, amine-modified DNA probe that binds to the
298 AAV2 genome. Nuclei were counterstained with DAPI (blue). (B) AAV2 capsid
299 proteins (green) were detected using an antibody (linear epitope) against VP1 and

VP2. AAV2 DNA (magenta) was detected by linking the amine-modified DNA to AF647. Nucleoli (Nuc) were visualized using an antibody against fibrillarin (yellow). Nuclei were counterstained with DAPI and illustrated as white lines.

Changes in nucleolar morphology correlate with cell cycle progression

To address the question whether the changes in nucleolar structure are linked to cell cycle progression, we performed image-based cell cycle analysis using DAPI and fibrillarin staining. To this end, a DAPI integrated intensity protocol was adapted from Ruokos et al. [35] and validated in NHF cells by correlating cyclin A, which is only expressed in late S and G2 cell cycle phases, with the integrated intensity of DAPI (S4 Fig; see also materials and methods). As a first step, the background of each image was subtracted (step 1). Next, nuclei as well as the cyclin A staining were identified as primary objects using CellProfiler (step 2). In step 3 and 4, nuclei and cyclin A were related to each other and the DAPI integrated intensity of each cell was measured. The measured properties of each individual cell were subsequently exported and read into Matlab, where histograms were plotted. Visual thresholds were set (red dotted lines) to distinguish the distribution of the histogram into G1, S and G2 (step 5). The images were then analyzed with a second CellProfiler pipeline using the visual thresholds of the integrated intensity of DAPI to classify cells into G1: 54.85%, S: 9.67% and G2: 35.48% (step 6). Lastly, overlay images, showing the cell cycle stage of each cell, were saved to allow the tracking of individual cells for further analysis (step 7).

To further validate the adapted protocol, NHF cells were synchronized using a double thymidine block. After the release, the cells were either mock-treated or

treated with nocodazole (200 nM) for 24 hours to induce a G2 cell cycle arrest. For flow cytometry, the cells were harvested, fixed and stained with DAPI. For CLSM, the coverslips were embedded in ProLong Anti-Fade mountant containing DAPI. Images were analyzed as described in the section cell cycle analysis based on 4`,6-diamidino-2-phenylindole (DAPI) staining. Both methods, flow cytometry and CLSM, showed a significant decrease of the number of cells within G1 cell cycle phase and a significant increase of cells in G2 cell cycle phase upon nocodazole treatment (S5 Fig), indicating that the adapted protocol is suitable for image-based cell cycle staging. Next, the fibrillarin staining was correlated to the cell cycle profile of the mock-infected and wtAAV2 infected NHF cells. Figure 6 shows that the ratios of dense to dispersed nucleoli decrease during cell cycle progression in both mock-infected and AAV2 infected cells. Overall, the data imply that the observed morphological changes of the nucleoli indeed coincide with cell cycle progression and were not due to AAV2-induced stress response (see also S3 Fig).

Fig 6. Nucleolar reorganization during cell cycle progression. Image-based analysis of the ratios of dense to dispersed nucleoli of 100 individual mock- or AAV2 infected cells in different cell cycle phases (G1, S and G2). p-values were calculated using an unpaired Student`s t-test (* - $p \leq 0.05$, ** - $p \leq 0.01$, *** - $p \leq 0.001$, **** - $p \leq 0.0001$).

G1 cell cycle phase obstructs complete AAV2 uncoating

Since we observed a decrease in the ratio of dense versus dispersed nucleolar structures (Fig 6 and S6 Fig) during cell cycle progression and a stronger intensity of AAV2 capsid signals in dense nucleoli than in dispersed nucleoli (Fig 4C), we next addressed the question whether cell cycle progression is important for complete

AAV2 uncoating. For this, NHF cells were arrested in the G1 phase by a double thymidine treatment before and during infection with wtAAV2 (MOI 20`000). As control, the cells were released 8 h prior to infection by washing out the thymidine. At 24 h after infection, there was a robust difference in the cell cycle profile between G1-arrested cells (approx. 83 % in G1) and released cells (approx. 47% in G1), confirming the efficient G1 arrest (Fig 7A). Image-based cell cycle analysis showed that the rate of complete uncoating (AAV2 capsid-DNA+/AAV2 capsid+DNA+) was approximately 4-fold lower in the G1-arrested cells compared to the released cells (Fig 7B). The double thymidine block did not *per se* influence the rate of complete uncoating, as the ratios of AAV2 capsid-DNA+/AAV2 capsid+DNA+ signals in G1 cells were comparable in presence or absence of thymidine (Fig 7C). Moreover, neither the blocking with nor the release from thymidine influenced the total area of the nucleoli during cell cycle progression (Fig 7D).

Fig 7. G1 cell cycle arrest obstructs complete uncoating. NHF cells were arrested in G1 cell cycle phase by a double thymidine block before and during infection with wtAAV2 (MOI 20`000). As control, the cells were released 8 h prior to infection by washing out the thymidine. At 24 hpi, the cells were fixed and processed for multicolor IF analysis combined with FISH, CLSM and image-based analysis of (A) the cell cycle profile after continuous thymidine block or release, respectively. (B) Quantification of the total uncoating rate. (C) Image-based quantification of the uncoating rate in G1 cell cycle phase. (D) Image-based quantification of the nucleolar area after continuous thymidine block or release, respectively. p-values were calculated using an unpaired Student`s t-test (* - $p \leq 0.05$, ** - $p \leq 0.01$, *** - $p \leq 0.001$, **** - $p \leq 0.0001$).

Induction of nucleolar disruption overcomes thymidine-mediated obstruction of AAV2 uncoating

NHF cells were arrested in the G1 phase of the cell cycle by a double thymidine block before and during infection with wtAAV2 (MOI 20`000). At 24 hpi, the cells were treated with actinomycin D (50 nM) for 1 h in order to induce nucleolar disruption (reviewed in [36]), fixed and processed for multicolor IF-FISH and CLSM (Fig 8A). Analysis of the cell cycle profile confirmed the cell cycle arrest upon thymidine and actinomycin D treatment (60% of cells in G1). The actinomycin D mediated nucleolar disruption in thymidine-treated cells led to a considerable decrease of capsid signals in the nucleoli and nucleoplasm and an increase of AAV2 genome signals in the nucleoplasm (Fig 8, A and B). This shows that complete uncoating can be induced by changes in the nucleolar structure (disruption) even when cells are in G1 phase where normally no efficient complete uncoating is observed (Fig 7).

Fig 8. Actinomycin D treatment overcomes thymidine-mediated obstruction of AAV2 uncoating. NHF cells were arrested in G1 cell cycle phase by a double thymidine block before and during infection with wtAAV2 (MOI 20`000). At 24 hpi, the cells were treated with actinomycin D for 1 h, fixed and processed for multicolor IF analysis combined with FISH and CLSM. (A) Nucleoli (Nuc) were visualized using an antibody against fibrillarin (yellow). Intact capsids were stained using an antibody that detects a conformational capsid epitope (green). AAV2 DNA (red) was detected with an Alexa Fluor (AF) 647 labeled, amine-modified DNA probe that binds to the AAV2 genome. (B) Image-based quantification of 50 individual cells per condition for

nucleolar capsid, total nuclear capsid or total nuclear AAV2 genome signals. p-values were calculated using an unpaired Student`s t-test (* - $p \leq 0.05$, ** - $p \leq 0.01$, *** - $p \leq 0.001$, **** - $p \leq 0.0001$).

Capsid disassembly coincides with cell cycle progression

To further assess whether capsid disassembly overlaps with cell cycle progression, NHF cells were either mock-infected or infected with wtAAV2 (MOI 20`000). 24 h later, the cells were fixed and processed for IF-FISH, CLSM and image-based cell cycle analysis and quantification. Specifically, we used the DAPI integrated intensity protocol to determine the cell cycle phase and the IF-FISH protocol to detect intact AAV2 capsids, the disassembled AAV2 VP1/2/3 capsid proteins, and the AAV2 DNA (Fig 9). In 55% of the cells in G1 cell cycle phase but only in 29% of the cells in S/G2 we observed the accumulation of AAV2 DNA together with AAV2 capsids (genome accessibility). In contrast, the number of cells in which the AAV2 DNA did not accumulate together with AAV2 capsids but rather with AAV2 capsid proteins VP1, VP2 and VP3 (complete uncoating) increased from 50% in G1 to 80% in S/G2. The same observation held true for neonatal human dermal fibroblasts (HDFn) cells infected with wtAAV2 (S7 Fig). Overall, our data strongly indicate that capsid disassembly coincides with cell cycle progression and nucleolar alterations.

Fig 9. Capsid disassembly coincides with cell cycle progression. NHF cells were infected with wtAAV2 (MOI 20`000). At 24 hpi, the cells were fixed and processed for multicolor IF analysis combined with FISH and CLSM. (A) Intact capsids (green) or capsid proteins (yellow) were detected using either an antibody against intact AAV2 capsids (conformational capsid epitope) or an antibody (linear epitope) against VP1, VP2 and VP3. AAV2 DNA (magenta) was detected with an

Alexa Fluor (AF) 647 labeled, amine-modified DNA probe that binds to the AAV2 genome. Nuclei were counterstained with DAPI and illustrated as white lines. (B) Quantification of at least 70 nuclei positive for intact AAV2 capsids or capsid proteins during cell cycle progression.

Discussion

Nucleoli are membrane-less and dynamic subnuclear structures, which were mainly known for their role in ribosome biosynthesis. However, nucleoli have a function in numerous other cellular processes as well, such as cell cycle regulation, stress response and apoptosis (reviewed in [16–19]). Proteomic approaches led to the identification of roughly 4`500 nucleolar associated proteins of which only a third is linked to ribosome biogenesis [37,38].

Many different viruses can exploit the nucleolus or nucleolar proteins to drive different steps of their life cycle including replication, transcription, and assembly (reviewed in [20,21,39,40]). For example, HSV-1 induces the redistribution of nucleolin from the nucleolus into HSV-1 replication compartments in a ICP4-dependent manner, thereby leading to enhanced HSV-1 replication and disruption of the nucleolar structure [41]. Similarly, nucleolar upstream binding factor (UBF) and nucleophosmin (B23.1) are recruited to adenovirus replication compartments to promote viral DNA replication [42–44]. The autonomous parvovirus minute virus of mice has been shown to replicate its DNA in the nucleoli of mouse fibroblasts [45,46]. Additionally, borna disease virus transcription and replication take place in the nucleoli as well [47]. Moreover, specific mRNAs and proteins of many different viruses, including HIV-1, Japanese encephalitis virus, and Semliki Forest virus traffic through the nucleolus for processing, and the inhibition of such trafficking affects virus replication [48–50].

Helper virus-supported AAV2 DNA replication occurs in nuclear replication compartments that are distinctly separate from nucleoli (S8 Fig). However, AAV2 interacts with nucleoli at both early and late stages of the replication cycle, cell entry and assembly. Upon nuclear entry AAV2 capsids have been shown to accumulate in the nucleoli [14,15]. Later in infection, intact AAV2 capsids were detected also in the nucleoplasm. Treatment of cells with hydroxyurea or proteasome inhibitors, both of which are known to improve AAV2 transduction efficiency, increased either nucleolar accumulation of AAV2 capsids or their relocalization into the nucleoplasm. Moreover, the post-transcriptional silencing of nucleophosmin enhanced nucleolar accumulation and increased transduction comparable to the proteasome inhibitor treatment, while the siRNA-mediated silencing of nucleolin mobilized capsids to the nucleoplasm and enhanced transduction similar to the treatment with hydroxyurea. These observations led to the hypothesis that AAV2 uncoating takes place in the nucleoplasm [22]. However, in the afore mentioned study and all other studies, viral capsids and viral genomes were not directly correlated on the single cell level but rather analyzed by quantitative (q)PCR, Western blot and immunofluorescence [22,24–27,29–31].

By employing combined immunofluorescence analysis with fluorescence *in situ* hybridization (IF-FISH) and confocal laser scanning microscopy, we monitored the spatial and temporal distribution of AAV2 capsids and genomes on the single cell level and observed that AAV2 DNA accumulates together with AAV2 capsids in the nucleoli of AAV2 infected cells, thereby confirming previous findings that the nucleolus acts as a sink for incoming AAV2 particles. In addition, our IF-FISH assay provides evidence for the stepwise uncoating of the AAV2 particle. Step 1 occurs in the cytoplasm and leads to AAV2 genome accessibility where the viral capsid is still recognized by an antibody that binds to a conformational capsid epitope and co-localizes with AAV2 DNA. Step 2 takes place within the nucleoli and results in the

complete disassembly of the AAV2 capsids and the accumulation of AAV2 DNA and AAV2 capsid proteins.

The exact mechanism that drives step 1 of the AAV2 uncoating process remains to be investigated. However, our data show that it is enhanced by acidification, as co-detection of AAV2 capsids and AAV2 DNA in the cytoplasm was reduced in cells treated with bafilomycin A1, a vacuolar H+-ATPase inhibitor. The interaction of importin β and the N-terminal end of VP1 [24] as well as the pH-dependent structural reorganization of the AAV2 capsid leading to the extrusion of the nuclear localization signals located in $VP1_u$ and VP1/VP2 N-termini [13,51,52] have been shown to be relevant for efficient nuclear entry of the AAV2 capsid. Whether or not the accessibility of the AAV2 genome for the AAV2 DNA specific FISH probe in AAV2 capsids that are still recognized by a conformational capsid antibody is due to pH-dependent structural rearrangements of the capsid or rather due to the protrusion of the AAV2 DNA from an almost intact AAV2 capsid, as it has been shown for thermally induced AAV2 genome release [53], requires further investigation. The accessibility of the AAV2 genome, however, might provide further evidence for the Toll-like receptor 9 (TLR9) mediated antiviral activation state in AAV2 infected untransformed cells [54].

Our image-based analysis of the nucleolar structure as well as AAV2 DNA, AAV2 capsids, and AAV2 capsid proteins, relative to the cell cycle profile provides strong evidence that step 2 of the uncoating process, the complete disassembly of the capsid, occurs in the nucleolus. The data also support the hypothesis that the complete disassembly of AAV2 capsids is induced by the structural reorganization of the nucleolus in a cell cycle-dependent manner.

While it is common for viruses to take advantage of the cell cycle or to undermine it in order to drive different stages of their life cycle (reviewed in [55]), little is known

about viruses availing the cell cycle to drive their uncoating process. A recent study demonstrated that the HIV-1 is unable to uncoat its core in quiescent CD4+ lymphocytes and that the uncoating activity requires transition from G0/$G1_a$ to $G1_b$ stage, arguing for the demand of cell cycle-dependent specific factors for HIV-1 uncoating [56]. For foamy virus (FV), capsid uncoating and the formation of the preintegration complex starts with the onset of mitosis. As the microtubule organizing center and the associated centrosomes, both being relevant for the life cycle of the virus, are highly linked to cell cycle regulation, it is likely that cell cycle regulatory proteins might contribute to FV capsid uncoating [57].

Nucleolar proteins such as nucleolin can bind to AAV2 capsids and seem to play a major role in the AAV2 replication cycle. Several studies demonstrated that nucleolin is barely detectable in resting cells; in contrast, nucleolin represents the major nucleolar protein in cycling eukaryotic cells [23,58]. This observation provides evidence for a link between AAV2 capsids, cell cycle progression and nucleolar proteins.

The interaction of some virus proteins with the nucleoli has been shown to be regulated by the cell cycle as well. For example, the human cytomegalovirus UL83 protein and the coronavirus nucleocapsid protein have been shown to localize to the nucleolus preferentially in the G1 and the G2 phase of the cell cycle, respectively. Most interestingly, we have previously reported that AAV2 gene expression and DNA replication occur primarily in the G2 phase of the cell cycle [59]. This cell cycle-dependence was not due to inefficient second-strand synthesis in cells in G1 nor to cell cycle-dependent DNA damage responses, as gene expression from a double-stranded self-complementary AAV2 vector was also reliant on cells in the G2 phase of the cell cycle and the inhibition of specific kinases in DNA damage signaling did not

result in a shift of gene expression to cells in G1. Moreover, AAV2 transduction efficiency was shown to be lower in quiescent cells compared to proliferating cells [60] Based on our new finding that the accumulation of AAV2 DNA together with disassembled AAV2 capsid proteins in dispersed nucleoli coincides with the G2 phase of the cell cycle, it is tempting to speculate that cell cycle-dependent AAV2 gene expression and DNA replication is controlled by cell cycle-dependent reorganization of the nucleolar structure that enables AAV2 uncoating. This hypothesis is further supported by the observation that perturbations that lead to changes in the nucleolar architecture such as actinomycin D treatment (this study), helper virus infection, or post-transcriptional silencing of nucleolin, enhance AAV2 transduction. However, the exact mechanism of the disassembly of the AAV2 capsid by nucleolar reorganization during cell cycle progression remains to be further investigated.

Materials and methods

Cells and viruses

Normal human fibroblast (NHF) cells were kindly provided by X.O. Breakefield (Massachusetts General Hospital, Charlestown, MA, USA). NHF cells, neonatal human dermal fibroblast cell line HDFn (ATCC PCS-201-010, American Type Culture Collection, Rockville, Md, USA) and African green monkey kidney cells (Vero cells, ATCC, American Type Culture Collection, Rockville, Md, USA) were maintained in growth medium containing Dulbecco's modified Eagle medium (DMEM) supplemented with 10% fetal bovine serum (FBS), 100 U/ml penicillin G, 100 µg/ml streptomycin, and 0.25 µg/ml amphotericin B (1% AB) at 37°C in a 95% air-5% CO_2 atmosphere. Wild-type (wt) AAV2 was produced by H. Buening (University of Hannover, Hannover, Germany) and the Viral Vector Facility (VVF) of the

553 Neuroscience Center Zurich (ZNZ). The VP1 AAV2 mutant (^{76}HD/AN) was
554 constructed according to Girod et al. [33] and produced by the VVF.
555 Briefly, the ^{76}HD/AN mutant construct was generated by mutating two key residues
556 ^{76}HD to ^{76}AN using K-^{76}HD/AN (5`GCGGCCCTCGAGGCCAACAAAGCCTACGACCGG
557 3`), L-$^{76}$HD/AN (5` CCGGTCGTAGGCTTTGTTGGCCTCGAGGGCCGC 3`), p*sub*-201
558 [61] containing the full-length AAV2 genome as template and the QuikChange Site-
559 Directed Mutagenesis Kit (Agilent Technologies).

560 Antibodies

561 The following primary antibodies were used: anti-AAV2 intact particle (A20, ProGen;
562 dilution for Immunofluorescence [IF] 1:50), anti-AAV VP1/VP2/VP3 (VP51, ProGen,
563 dilution for IF 1:10), anti-AAV VP1/VP2 (A69, ProGen, dilution for IF 1:10), anti-AAV2
564 Rep (Fitzgerald Industries, 10R-A111A, dilution for IF 1:10), anti-fibrillarin (Abcam
565 ab5821; dilution for IF 1:200), anti-cyclin A (Santa Cruz sc-751, dilution for IF 1:500).
566 The following secondary antibodies were used: Alexa Fluor 594 goat anti-rabbit IgG
567 (Life Technologies A11037, dilution for IF 1:500), Alexa Fluor 488 goat anti-mouse IgG
568 (Invitrogen A11001, dilution for IF 1:500).

569 Viral infection and treatments

570 NHF, HDFn or Vero cells were seeded onto coverslips (12-mm diameter;
571 Glaswarenfabrik Karl Hecht GmbH & Co. KG, Sondheim, Germany) in 24-well tissue
572 culture plates at a density of $3x10^4$ cells per well. The next day the cells were washed
573 with PBS and either mock-infected or infected with wtAAV2 at a multiplicity of
574 infection (MOI) of 20`000 genome containing particles (gcp) per cell in 250 µl of
575 DMEM (0% FBS, 1% AB) pre-cooled to 4°C. The plates were first incubated for
576 30 min at 4°C to synchronize viral uptake and then incubated at 37°C in a humidified
577 95% air-5% CO_2 incubator for the indicated time period. For acidification experiments

NHF cells were treated with bafilomycine A1 (50 or 200 nM) or DMSO in DMEM (10% FBS, 1% AB) 1 h prior to infection with wtAAV2. G1 cell cycle phase arrest prior to infection was induced by a double thymidine block. For this, cells were seeded in 10 cm tissue culture dishes ($5x10^5$ cells per dish) and 12 h later the growth medium was replaced with medium (DMEM, 10% FBS, 1% AB) containing 3 mM thymidine. After 12 h of incubation, the cells were washed with PBS, trypsinized and split at a density of $6x10^4$ cells per well into 6-well tissue culture plates containing coverslips. In order to complete the double thymidine block, the growth medium was replaced 12 hours later by medium containing 3 mM thymidine. After 12 hours, the cells were either released from the block by washing out the thymidine with PBS or directly infected with wtAAV2 in the presence of thymidine. Nucleolar disruption was induced with actinomycin D (50 nM) in DMEM (2% FBS, 1% AB) for 1 h after 24 h of infection in presence of thymidine.

Cell cycle analysis based on 4`,6-diamidino-2-phenylindole (DAPI) staining

The workflow described is closely related and adapted from the protocol published by Roukos et al., 2015 ([62]). Briefly, NHF cells were seeded onto coverslips (12-mm diameter; Glaswarenfabrik Karl Hecht GmbH & Co. KG, Sondheim, Germany) in 24-well tissue culture plates ($3x10^4$ cells per well). The next day, the cells were washed with PBS, processed as indicated in the results and the figure legends, counterstained with DAPI and imaged by confocal laser scanning microscopy (Leica SP8; Leica Microsystems, Wetzlar, Germany). An automated CellProfiler (V.2.2.0-V.4.0.7) pipeline measured the integrated intensity of DAPI. Next, the histograms of DAPI, corresponding to the DNA content, were plotted and visual thresholds for each cell cycle phase were selected. These thresholds were finally read back into a secondary

CellProfiler pipeline, which lastly allowed tracking of individual cells and measurements.

Comparison of cell cycle classification using flow cytometry and the DAPI integrated intensity protocol

To validate the DAPI integrated intensity protocol, NHF cells were synchronized using a double thymidine block (as described above). After the release, the cells were either mock-treated or treated with nocodazole (200 nM) for 24 hours. For flow cytometry, the cells were harvested by exposing them to 0.05 % Trypsin-EDTA solution for 10 min, centrifuged and washed with PBS, fixed in 2.5 ml ice-cold 100% ethanol, centrifuged, washed once again with PBS and stained with a freshly made solution containing 1 µg/mL DAPI, 0.05% Triton X-100 and 0.1 mg/mL ribonuclease A (RNase A) in PBS. All samples were incubated for 45 min at 37°C in the dark. After incubation, the cells were washed twice with PBS and then resuspended in 200 µl PBS prior to analysis (SONY SP6800 Spectral Analyzer). For confocal laser scanning microscopy, the coverslips were embedded in ProLong Anti-Fade mountant with DAPI (Molecular Probes, Eugene, OR, USA) and imaged using a 63x oil immersion objective (Leica SP8; Leica Microsystems, Wetzlar, Germany). Images were analyzed as described in the section cell cycle analysis based on 4`,6-diamidino-2-phenylindole (DAPI) staining.

Combined multicolor immunofluorescence analysis and fluorescence *in situ* hybridization (FISH)

FISH was performed essentially as described previously by Lux et al. [27]. Briefly, a 3.9-kb DNA fragment containing the AAV2 genome without the inverted terminal repeats was amplified by PCR from plasmid pDG using forward (5`-CGGGGTTTTACGAGATTGTG-3`) and reverse (5`-GGCTCTGAATACACGCCATT-3`) primers and the following conditions: 30 s at 95°C; 35 cycles of 10 s at 98°C, 15 s

at 58°C, and 75 s at 72°C; and 10 min at 72°C. The PCR sample was then digested with DpnI to cut the residual template DNA and purified with the Pure Link PCR purification kit (Qiagen, Hilden, Germany). The DNA fragment was labeled with 5-(3-aminoallyl)dUTP by nick translation according to the manufacturer's protocol (Ares DNA labeling kit, Molecular Probes, Eugene, OR, USA), and the incorporated dUTPs were labeled with amino-reactive Alexa Fluor 647 dye by using the same Ares DNA labeling kit. NHF cells were plated onto glass coverslips in 24-well tissue culture plates at a density of $3x10^4$ cells per well and 24 h later mock-infected or infected with wtAAV2 (MOI of 20`000). 24 hours after infection, the cells were washed with PBS, fixed for 30 min at room temperature (RT) with 2% PFA (in PBS), and washed again with PBS. The cells were then quenched for 10 min with 50 mM NH_4Cl (in PBS), washed with PBS, permeabilized for 10 min with 0.2% Triton X-100 (in PBS), blocked for 10 min with 0.2% gelatin (in PBS) followed by two washing steps with PBS before blocking for 30 min in PBST (0.05% Tween 20 in PBS) supplemented with 3% BSA at 4°C. After antibody staining in PBST-BSA (3%, 25 µl/coverslip) for 1h at RT in the dark in a humidified chamber, the cells were washed three times for 5 min with PBST (0.1%), post-fixed with 2% PFA and blocked with 50 mM glycine in PBS for 5 min at RT.

Hybridization solution (20 µl per coverslip) containing 1 ng/µl of the labeled DNA probe, 50% formamide, 7.3% (w/v) dextran sulfate, 15 ng/µl salmon sperm DNA, and 0.74x SSC (1x SSC is 0.15 M NaCl and 0.015 M sodium citrate) was denatured for 3 min at 95°C and shock-cooled on ice. The coverslips with the fixed and permeabilized cells facing down were placed onto a drop (20 µl) of the denatured hybridization solution and incubated overnight at 37°C in a humidified chamber (note that the cells were not denatured, as the AAV2 genome is present as ssDNA). The next day, the coverslips were washed three times with 2x SSC at 37°C, three times with 0.1x SSC at 60°C, and twice with PBS at RT. To confirm the FISH signal, some samples (as stated in the

results) were treated with DNase I (1U/ µl) for 1 h at 37°C followed by inactivation in 30% formamide, 0,1% Triton-X 100 and 2x SSC for 10 min at RT.

The cells were then embedded in ProLong Anti-Fade mountant with or without DAPI (Molecular Probes, Eugene, OR, USA) and imaged by confocal laser scanning microscopy (Leica SP8; Leica Microsystems, Wetzlar, Germany). To prevent cross talk between the channels for the different fluorochromes, all channels were recorded separately, and fluorochromes with longer wavelengths were recorded first. The resulting images were processed using Imaris V.7.7.2-V.9.6.0 (Bitplane, Oxford Instruments, Biplane AG, Zurich, Switzerland)

Negative contrast stain

For the examination of AAV2 capsid disintegration a negative contrast staining was performed. For this, 10 µl of the wtAAV2 stock were placed onto a parafilm strip and adsorbed to carbon coated parlodion films mounted on 300 mesh/inch copper grids by placing upside-down on the drop and incubated for 10min at RT. Washing was done by transferring the grid to a H_2O drop. Subsequently the grid was placed onto a drop of phosphotungstic acid (PTA, pH 7.0) for 60 seconds. Remaining liquid was removed by tipping the edge of the grid on a filter paper. The samples were analyzed in a Philips CM 12 transmission electron microscope (Eindhoven, the Netherlands) equipped with a charge-coupled device (CCD) camera (Ultrascan 1000, Gatan, Pleasanton, CA, USA) at an acceleration voltage of 100 kV.

Image-based quantification and data analysis

For image-based quantification and data analysis, at least 50 individual cells per sample or condition were recorded and analyzed using different CellProfiler (V.2.2.0-V.4.0.7) pipelines. The output csv-files were further analyzed using Matlab (R2017a) and GraphPad Prism 6 to 9. Depending on distribution frequency and standard

679 deviation (SD), statistical analysis of individual cells was either performed by unpaired
680 Student`s t-test or an unpaired t-test with Welch`s correction (not assuming equal
681 SDs). If not stated otherwise, each graph illustrates one representative experiment.
682

683 # References

684 1. Samulski RJ, Zhu X, Xiao X, Brook JD, Housman DE, Epstein N, et al. Targeted
685 integration of adeno-associated virus (AAV) into human chromosome 19. Embo J.
686 1991;10: 3941–3950. doi:10.1002/j.1460-2075.1991.tb04964.x

687 2. Sun X, Lu Y, Bish LT, Calcedo R, Wilson JM, Gao G. Molecular Analysis of Vector
688 Genome Structures After Liver Transduction by Conventional and Self-
689 Complementary Adeno-Associated Viral Serotype Vectors in Murine and Nonhuman
690 Primate Models. Hum Gene Ther. 2010;21: 750–761. doi:10.1089/hum.2009.214

691 3. Buller RM, Janik JE, Sebring ED, Rose JA. Herpes simplex virus types 1 and 2
692 completely help adenovirus-associated virus replication. Journal of Virology. 1981;40:
693 241–247.

694 4. Srivastava A, Lusby EW, Berns KI. Nucleotide sequence and organization of the
695 adeno-associated virus 2 genome. J Virol. 1983;45: 555–564.
696 doi:10.1128/jvi.45.2.555-564.1983

697 5. Laughlin CA, Westphal H, Carter BJ. Spliced adenovirus-associated virus RNA.
698 Proc National Acad Sci. 1979;76: 5567–5571. doi:10.1073/pnas.76.11.5567

699 6. Pereira DJ, McCarty DM, Muzyczka N. The adeno-associated virus (AAV) Rep
700 protein acts as both a repressor and an activator to regulate AAV transcription during

701 a productive infection. J Virol. 1997;71: 1079–1088. doi:10.1128/jvi.71.2.1079-
702 1088.1997

703 7. Sonntag F, Kother K, Schmidt K, Weghofer M, Raupp C, Nieto K, et al. The
704 assembly-activating protein promotes capsid assembly of different adeno-associated
705 virus serotypes. Journal of Virology. 2011;85: 12686–12697. doi:10.1128/jvi.05359-
706 11

707 8. Ogden PJ, Kelsic ED, Sinai S, Church GM. Comprehensive AAV capsid fitness
708 landscape reveals a viral gene and enables machine-guided design. Science.
709 2019;366: 1139–1143. doi:10.1126/science.aaw2900

710 9. Asokan A, Schaffer DV, Samulski RJ. The AAV Vector Toolkit: Poised at the
711 Clinical Crossroads. Mol Ther. 2012;20: 699–708. doi:10.1038/mt.2011.287

712 10. Nonnenmacher M, Weber T. Intracellular transport of recombinant adeno-
713 associated virus vectors. Gene therapy. 2012;19: 649–658. doi:10.1038/gt.2012.6

714 11. Pillay S, Meyer NL, Puschnik AS, Davulcu O, Diep J, Ishikawa Y, et al. An
715 essential receptor for adeno-associated virus infection. Nature. 2016;530: 108–112.
716 doi:10.1038/nature16465

717 12. Nonnenmacher M, Weber T. Adeno-associated virus 2 infection requires
718 endocytosis through the CLIC/GEEC pathway. Cell Host & Microbe. 2011;10: 563–
719 576. doi:10.1016/j.chom.2011.10.014

720 13. Stahnke S, Lux K, Uhrig S, Kreppel F, Hösel M, Coutelle O, et al. Intrinsic
721 phospholipase A2 activity of adeno-associated virus is involved in endosomal escape
722 of incoming particles. Virology. 2011;409: 77–83. doi:10.1016/j.virol.2010.09.025

14. Qiu J, Brown KE. A 110-kDa nuclear shuttle protein, nucleolin, specifically binds to adeno-associated virus type 2 (AAV-2) capsid. Virology. 1999;257: 373–382. doi:10.1006/viro.1999.9664

15. Bevington JM, Needham PG, Verrill KC, Collaco RF, Basrur V, Trempe JP. Adeno-associated virus interactions with B23/Nucleophosmin: identification of sub-nucleolar virion regions. Virology. 2007;357: 102–113. doi:10.1016/j.virol.2006.07.050

16. Olson MO, Dundr M, Szebeni A. The nucleolus: an old factory with unexpected capabilities. Trends in cell biology. 2000;10: 189–196.

17. Hernandez-Verdun D, Roussel P, Gébrane-Younès J. Emerging concepts of nucleolar assembly. Journal of cell science. 2002;115: 2265–2270.

18. Yang K, Yang J, Yi J. Nucleolar Stress: hallmarks, sensing mechanism and diseases. Cell Stress. 2018;2: 125–140. doi:10.15698/cst2018.06.139

19. Boulon S, Westman BJ, Hutten S, Boisvert F-M, Lamond AI. The nucleolus under stress. Molecular Cell. 2010;40: 216–227. doi:10.1016/j.molcel.2010.09.024

20. Matthews D, Emmott E, Hiscox J. The Nucleolus. 2011; 321–345. doi:10.1007/978-1-4614-0514-6_14

21. Salvetti A, Greco A. Viruses and the nucleolus: the fatal attraction. Biochimica et biophysica acta. 2014;1842: 840–847. doi:10.1016/j.bbadis.2013.12.010

22. Johnson JS, Samulski RJ. Enhancement of adeno-associated virus infection by mobilizing capsids into and out of the nucleolus. Journal of Virology. 2009;83: 2632–2644. doi:10.1128/jvi.02309-08

745 23. BUGLER B, CAIZERGUES-FERRER M, BOUCHE G, BOURBON H, AMALRIC
746 F. Detection and Localization of a Class of Proteins Immunologically Related to a
747 100-kDa Nucleolar Protein. Eur J Biochem. 1982;128: 475–480. doi:10.1111/j.1432-
748 1033.1982.tb06989.x

749 24. Nicolson SC, Samulski RJ. Recombinant adeno-associated virus utilizes host cell
750 nuclear import machinery to enter the nucleus. Journal of Virology. 2014;88: 4132–
751 4144. doi:10.1128/jvi.02660-13

752 25. Bartlett JS, Wilcher R, Samulski RJ. Infectious entry pathway of adeno-
753 associated virus and adeno-associated virus vectors. Journal of Virology. 2000;74:
754 2777–2785.

755 26. Kelich JM, Ma J, Dong B, Wang Q, Chin M, Magura CM, et al. Super-resolution
756 imaging of nuclear import of adeno-associated virus in live cells. Mol Ther - Methods
757 Clin Dev. 2015;2: 15047. doi:10.1038/mtm.2015.47

758 27. Lux K, Goerlitz N, Schlemminger S, Perabo L, Goldnau D, Endell J, et al. Green
759 fluorescent protein-tagged adeno-associated virus particles allow the study of
760 cytosolic and nuclear trafficking. Journal of Virology. 2005;79: 11776–11787.
761 doi:10.1128/jvi.79.18.11776-11787.2005

762 28. Bartlett JS, Wilcher R, Samulski RJ. Infectious entry pathway of adeno-
763 associated virus and adeno-associated virus vectors. Journal of Virology. 2000;74:
764 2777–2785.

765 29. Xiao W, Warrington KH, Hearing P, Hughes J, Muzyczka N. Adenovirus-
766 Facilitated Nuclear Translocation of Adeno-Associated Virus Type 2. J Virol. 2002;76:
767 11505–11517. doi:10.1128/jvi.76.22.11505-11517.2002

768 30. Sipo I, Fechner H, Pinkert S, Suckau L, Wang X, Weger S, et al. Differential
769 internalization and nuclear uncoating of self-complementary adeno-associated virus
770 pseudotype vectors as determinants of cardiac cell transduction. Gene Ther.
771 2007;14: 1319–1329. doi:10.1038/sj.gt.3302987

772 31. Zhong L, Li W, Yang Z, Qing K, Tan M, Hansen J, et al. Impaired Nuclear
773 Transport and Uncoating Limit Recombinant Adeno-Associated Virus 2 Vector-
774 Mediated Transduction of Primary Murine Hematopoietic Cells. Hum Gene Ther.
775 2004;15: 1207–1218. doi:10.1089/hum.2004.15.1207

776 32. Wistuba A, Kern A, Weger S, Grimm D, Kleinschmidt JA. Subcellular
777 compartmentalization of adeno-associated virus type 2 assembly. J Virol. 1997;71:
778 1341–1352. doi:10.1128/jvi.71.2.1341-1352.1997

779 33. Girod A, Wobus CE, Zádori Z, Ried M, Leike K, Tijssen P, et al. The VP1 capsid
780 protein of adeno-associated virus type 2 is carrying a phospholipase A2 domain
781 required for virus infectivity. The Journal of general virology. 2002;83: 973–978.
782 doi:10.1099/0022-1317-83-5-973

783 34. Rayaprolu V, Kruse S, Kant R, Venkatakrishnan B, Movahed N, Brooke D, et al.
784 Comparative Analysis of Adeno-Associated Virus Capsid Stability and Dynamics. J
785 Virol. 2013;87: 13150–13160. doi:10.1128/jvi.01415-13

786 35. Roukos V, Pegoraro G, Voss TC, Misteli T. Cell cycle staging of individual cells
787 by fluorescence microscopy. Nature protocols. 2015;10: 334–348.
788 doi:10.1038/nprot.2015.016

789 36. Latonen L. Phase-to-Phase With Nucleoli – Stress Responses, Protein
790 Aggregation and Novel Roles of RNA. Front Cell Neurosci. 2019;13: 151.
791 doi:10.3389/fncel.2019.00151

792 37. Ahmad Y, Boisvert F-M, Gregor P, Cobley A, Lamond AI. NOPdb: Nucleolar
793 Proteome Database—2008 update. Nucleic Acids Res. 2009;37: D181–D184.
794 doi:10.1093/nar/gkn804

795 38. Lindström MS, Jurada D, Bursac S, Orsolic I, Bartek J, Volarevic S. Nucleolus as
796 an emerging hub in maintenance of genome stability and cancer pathogenesis.
797 Oncogene. 2018;37: 2351–2366. doi:10.1038/s41388-017-0121-z

798 39. Hiscox JA. The nucleolus – a gateway to viral infection? Arch Virol. 2002;147:
799 1077–1089. doi:10.1007/s00705-001-0792-0

800 40. Hiscox JA. RNA viruses: hijacking the dynamic nucleolus. Nat Rev Microbiol.
801 2007;5: 119–127. doi:10.1038/nrmicro1597

802 41. Callé A, Ugrinova I, Epstein AL, Bouvet P, Diaz J-J, Greco A. Nucleolin is
803 required for an efficient herpes simplex virus type 1 infection. Journal of Virology.
804 2008;82: 4762–4773. doi:10.1128/jvi.00077-08

805 42. Hindley CE, Davidson AD, Matthews DA. Relationship between adenovirus DNA
806 replication proteins and nucleolar proteins B23.1 and B23.2. J Gen Virology.
807 2007;88: 3244–3248. doi:10.1099/vir.0.83196-0

808 43. Lawrence FJ, McStay B, Matthews DA. Nucleolar protein upstream binding factor
809 is sequestered into adenovirus DNA replication centres during infection without

affecting RNA polymerase I location or ablating rRNA synthesis. J Cell Sci. 2006;119: 2621–2631. doi:10.1242/jcs.02982

44. Okuwaki M, Iwamatsu A, Tsujimoto M, Nagata K. Identification of nucleophosmin/B23, an acidic nucleolar protein, as a stimulatory factor for in vitro replication of adenovirus DNA complexed with viral basic core proteins11Edited by T. Richmond. J Mol Biol. 2001;311: 41–55. doi:10.1006/jmbi.2001.4812

45. Walton TH, Moen PT, Fox E, Bodnar JW. Interactions of minute virus of mice and adenovirus with host nucleoli. J Virol. 1989;63: 3651–3660. doi:10.1128/jvi.63.9.3651-3660.1989

46. Moen PT, Fox E, Bodnar JW. Adenovirus and minute virus of mice DNAs are localized at the nuclear periphery. Nucleic Acids Res. 1990;18: 513–520. doi:10.1093/nar/18.3.513

47. Pyper JM, Clements JE, Zink MC. The nucleolus is the site of Borna disease virus RNA transcription and replication. Journal of Virology. 1998;72: 7697–7702.

48. Michienzi A, Cagnon L, Bahner I, Rossi JJ. Ribozyme-mediated inhibition of HIV 1 suggests nucleolar trafficking of HIV-1 RNA. Proc National Acad Sci. 2000;97: 8955–8960. doi:10.1073/pnas.97.16.8955

49. Mori Y, Okabayashi T, Yamashita T, Zhao Z, Wakita T, Yasui K, et al. Nuclear Localization of Japanese Encephalitis Virus Core Protein Enhances Viral Replication†. J Virol. 2005;79: 3448–3458. doi:10.1128/jvi.79.6.3448-3458.2005

830 50. Fazakerley JK, Boyd A, Mikkola ML, Kääriäinen L. A Single Amino Acid Change
831 in the Nuclear Localization Sequence of the nsP2 Protein Affects the Neurovirulence
832 of Semliki Forest Virus. J Virol. 2002;76: 392–396. doi:10.1128/jvi.76.1.392-396.2002

833 51. Grieger JC, Snowdy S, Samulski RJ. Separate Basic Region Motifs within the
834 Adeno-Associated Virus Capsid Proteins Are Essential for Infectivity and Assembly. J
835 Virol. 2006;80: 5199–5210. doi:10.1128/jvi.02723-05

836 52. Sonntag F, Bleker S, Leuchs B, Fischer R, Kleinschmidt JA. Adeno-associated
837 virus type 2 capsids with externalized VP1/VP2 trafficking domains are generated
838 prior to passage through the cytoplasm and are maintained until uncoating occurs in
839 the nucleus. Journal of Virology. 2006;80: 11040–11054. doi:10.1128/jvi.01056-06

840 53. Bernaud J, Rossi A, Fis A, Gardette L, Aillot L, Büning H, et al. Characterization
841 of AAV vector particle stability at the single-capsid level. J Biol Phys. 2018;44: 181–
842 194. doi:10.1007/s10867-018-9488-5

843 54. Laredj LN, Beard P. Adeno-Associated Virus Activates an Innate Immune
844 Response in Normal Human Cells but Not in Osteosarcoma Cells. J Virol. 2011;85:
845 13133–13143. doi:10.1128/jvi.05407-11

846 55. Fan Y, Sanyal S, Bruzzone R. Breaking Bad: How Viruses Subvert the Cell
847 Cycle. Front Cell Infect Mi. 2018;8: 396. doi:10.3389/fcimb.2018.00396

848 56. Auewarakul P, Wacharapornin P, Srichatrapimuk S, Chutipongtanate S,
849 Puthavathana P. Uncoating of HIV-1 requires cellular activation. Virology. 2005;337:
850 93–101. doi:10.1016/j.virol.2005.02.028

851 57. Berka U, Hamann MV, Lindemann D. Early Events in Foamy Virus—Host
852 Interaction and Intracellular Trafficking. Viruses. 2013;5: 1055–1074.
853 doi:10.3390/v5041055

854 58. Lapeyre B, Bourbon H, Amalric F. Nucleolin, the major nucleolar protein of
855 growing eukaryotic cells: an unusual protein structure revealed by the nucleotide
856 sequence. Proc National Acad Sci. 1987;84: 1472–1476.
857 doi:10.1073/pnas.84.6.1472

858 59. Franzoso FD, Seyffert M, Vogel R, Yakimovich A, Pereira B de A, Meier AF, et al.
859 Cell Cycle-Dependent Expression of Adeno-Associated Virus 2 (AAV2) Rep in
860 Coinfections with Herpes Simplex Virus 1 (HSV-1) Gives Rise to a Mosaic of Cells
861 Replicating either AAV2 or HSV-1. Journal of Virology. 2017;91.
862 doi:10.1128/jvi.00357-17

863 60. Zhang L, Rossi A, Lange L, Meumann N, Koitzsch U, Christie K, et al. Capsid
864 Engineering Overcomes Barriers Toward Adeno-Associated Virus Vector-Mediated
865 Transduction of Endothelial Cells. Hum Gene Ther. 2019;30: 1284–1296.
866 doi:10.1089/hum.2019.027

867 61. Samulski RJ, Chang LS, Shenk T. A recombinant plasmid from which an
868 infectious adeno-associated virus genome can be excised in vitro and its use to study
869 viral replication. J Virol. 1987;61: 3096–3101. doi:10.1128/jvi.61.10.3096-3101.1987

870 62. Roukos V, Pegoraro G, Voss TC, Misteli T. Cell cycle staging of individual cells
871 by fluorescence microscopy. Nat Protoc. 2015;10: 334–348.
872 doi:10.1038/nprot.2015.016

873

Supporting information

S1 Fig. Endosomal escape is relevant for nucleolar accumulation. NHF cells were either mock-infected or infected with wtAAV2 or a VP1 AAV2 mutant (^{76}HD/AN) at a MOI of 20`000. At 5 hpi, the samples were processed for IF-FISH and CLSM. Intact capsids were stained using an antibody that detects a conformational capsid epitope (green). AAV2 DNA (red) was detected with an Alexa Fluor (AF) 647 labeled, amine-modified DNA probe that binds to the AAV2 genome. Nuclei were counterstained with DAPI (blue).

S2 Fig. Co-detection of AAV2 DNA with AAV2 capsids and AAV2 capsid proteins in Vero cells. Vero cells were infected with wtAAV2 (MOI 20`000). At 24 hpi, the cells were fixed and processed for multicolor IF analysis combined with FISH and CLSM. Intact capsids (green) or capsid proteins (yellow) were detected using either an antibody against intact AAV2 capsids (conformational capsid epitope) or an antibody (linear epitope) against VP1, VP2 and VP3. AAV2 DNA (red) was detected with an Alexa Fluor (AF) 647 labeled, amine-modified DNA probe that binds to the AAV2 genome. Nuclei were counterstained with DAPI (blue).

S3 Fig. AAV2 infection does not alter the ratio of dense to dispersed nucleoli. NHF cells were mock-infected or infected with wtAAV2 (MOI 20`000) and 24 h later processed for combined IF-FISH, CLSM and quantification of the nucleolar structure of 100 individual nuclei in mock- or AAV2 infected cells. p-values were calculated using an unpaired Student`s t-test (* - $p \leq 0.05$, ** - $p \leq 0.01$, *** - $p \leq 0.001$, **** - $p \leq 0.0001$).

S4 Fig. Schematic representation of the cell cycle staging by cyclin A staining and the integrated intensity of DAPI. (1) The background of each image was subtracted. (2) Nuclei and cyclin A stainings were identified as primary objects in CellProfiler. (3) The stainings were related to each other and (4) the DAPI integrated intensity of each nucleus was measured. (5) Histograms of the DAPI integrated intensities were plotted using an automated script in Matlab and visual thresholds were set. (6) Cells were classified in CellProfiler using the visual thresholds obtained in step 5. (7) The classification of each nucleus into G1, S or G2 was overlayed on the original DAPI image to track individual cells.

S5 Fig. Cell cycle staging of DAPI stained cells using flow cytometry analysis and confocal laser scanning microscopy. NHF cells were synchronized using a double thymidine (3 mM) block. After the release, the cells were either mock-treated or treated with nocodazole (200 nM) for 24 hours to induce a G2 cell cycle phase arrest. Flow cytometry shows the mean value of three experiments, each replicate contains at least 5`000 scored events. CLSM analysis shows the mean value of three experiments, each replicate contains at least 100 individual analyzed cells. p-values were calculated using an unpaired Student`s t-test (* - $p \leq 0.05$, ** - $p \leq 0.01$, *** - $p \leq 0.001$, **** - $p \leq 0.0001$).

S6 Fig. Nucleolar reorganization during cell cycle progression. Image-based analysis of the ratios of dense to dispersed nucleoli of 150 individual cells in different cell cycle phases (G1, S and G2). Statistical analysis was performed on three independent experiments and p-values were calculated using an unpaired Student`s t-test (* - $p \leq 0.05$, ** - $p \leq 0.01$, *** - $p \leq 0.001$, **** - $p \leq 0.0001$).

S7 Fig. Capsid disassembly coincides with cell cycle progression in HDFn cells. HDFn cells were infected with wtAAV2 (MOI 20`000). At 24 hpi, the cells were fixed and processed for multicolor IF analysis combined with FISH, CLSM. (A) Intact capsids (green) or capsid proteins (yellow) were detected using either an antibody against intact AAV2 capsids (conformational capsid epitope) or an antibody (linear epitope) against VP1, VP2 and VP3. AAV2 DNA (magenta) was detected with an Alexa Fluor (AF) 647 labeled, amine-modified DNA probe that binds to the AAV2 genome. Nuclei were counterstained with DAPI and illustrated as white lines. (B) Quantification of at least 50 nuclei positive for intact AAV2 capsids or capsid proteins during cell cycle progression.

S8 Fig. Helper virus-supported AAV2 DNA replication occurs in nuclear replication compartments that are distinctly separate from nucleoli. NHF cells were mock-infected or infected with wtAAV2 (MOI 10`000), HSV-1 (MOI 0.5) or co-infected with wtAAV2 (MOI 5`000) and HSV-1 (MOI 0.5). At 12 hpi, the cells were fixed and processed for multicolor IF analysis combined with FISH and CLSM. Nucleoli (Nuc) were visualized using an antibody against fibrillarin (yellow). wtAAV2 replication compartments were stained using a primary antibody specific for the AAV2 Rep proteins (green). AAV2 DNA (red) was detected with an Alexa Fluor (AF) 647 labeled, amine-modified DNA probe that binds to the AAV2 genome. Nuclei were counterstained with DAPI and illustrated as blue lines.

S1 Movie. Maximum intensity projection of AAV2 genome positive nucleoli. NHF cells were infected with wtAAV2 (MOI 20`000). At 24 hpi, the cells were fixed and processed for multicolor IF analysis combined with FISH and CLSM. Nucleoli were visualized using an antibody against fibrillarin (yellow). Intact capsids were

951 stained using an antibody that detects a conformational capsid epitope (green).
952 AAV2 DNA (red) was detected with an Alexa Fluor (AF) 647 labeled, amine-modified
953 DNA probe that binds to the AAV2 genome. Reconstructions were generated using
954 Imaris V.9.6.

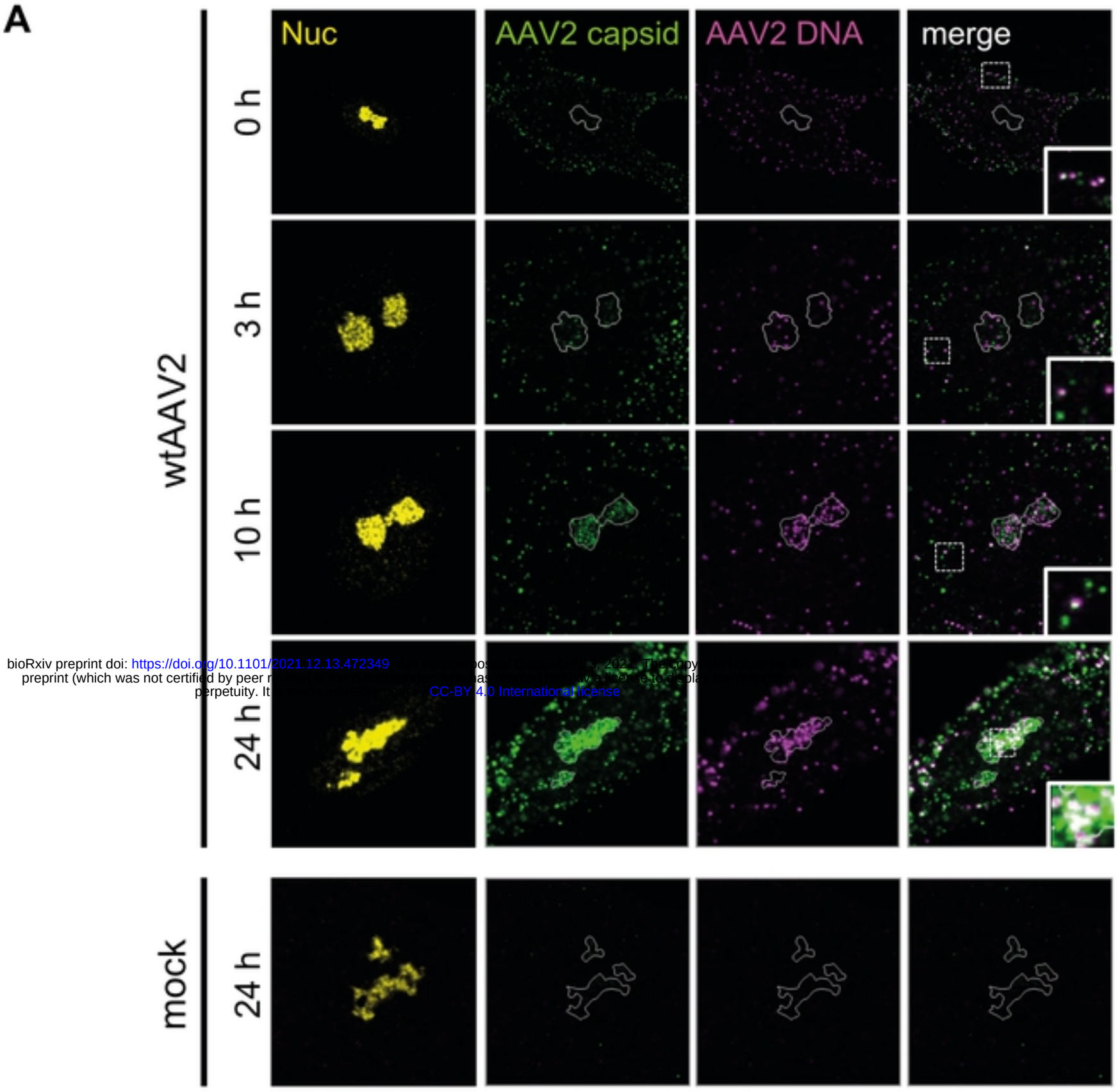

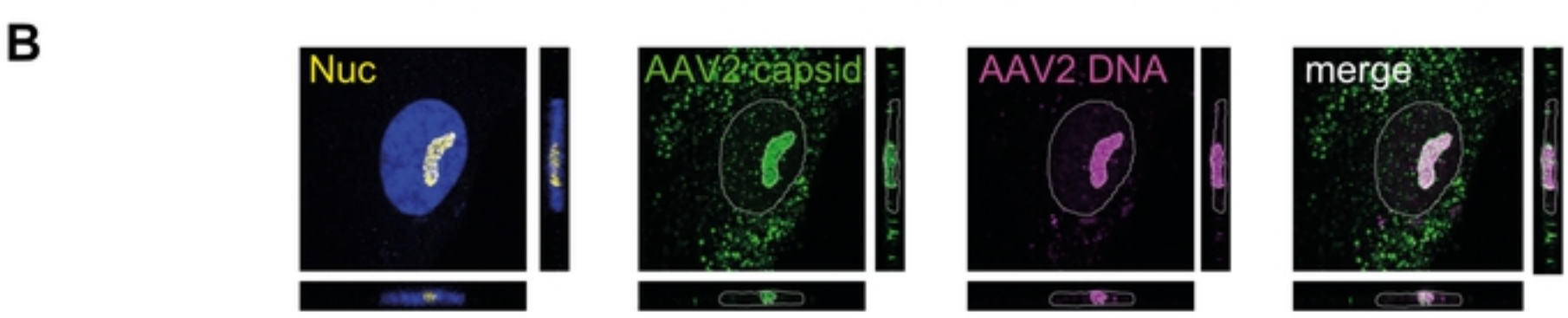

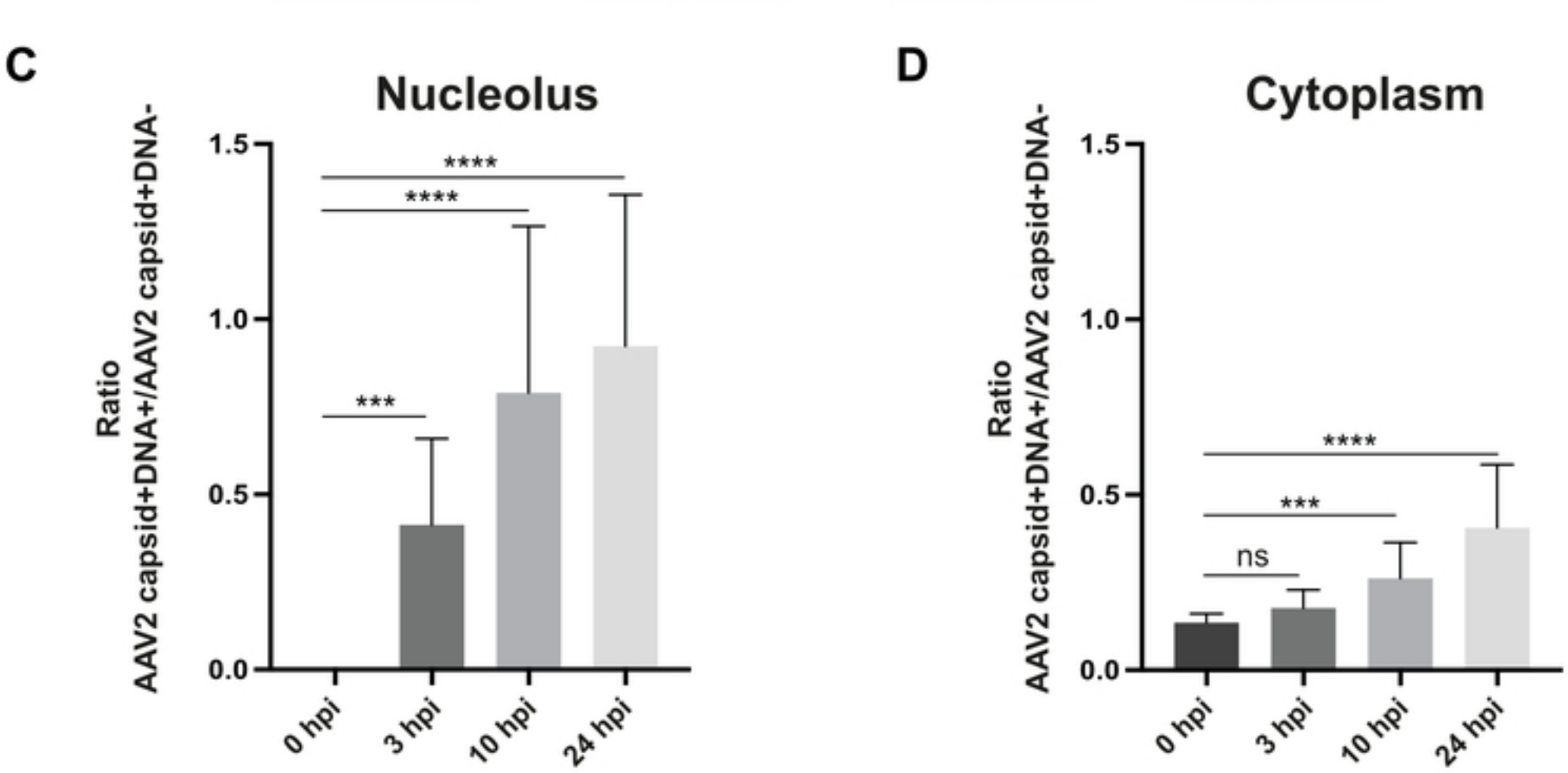

Fig1

A

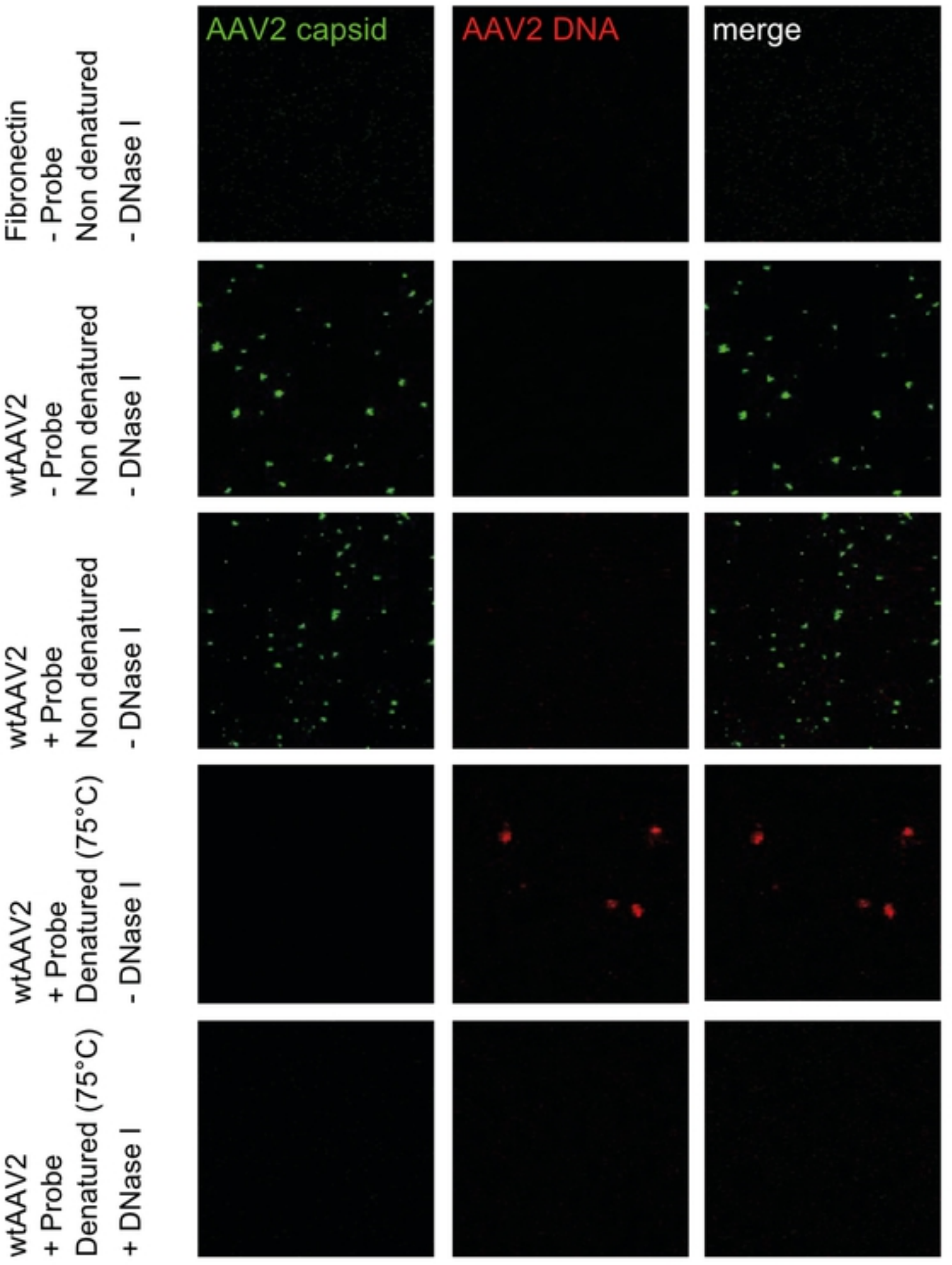

B

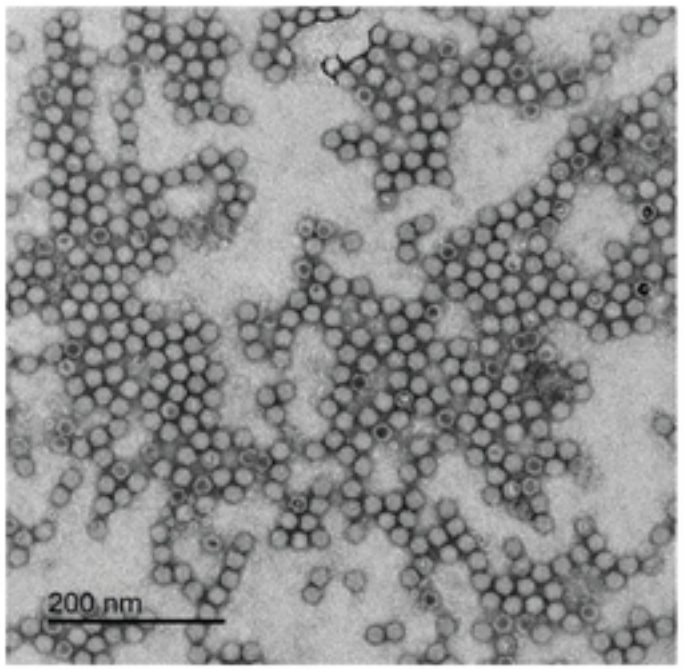

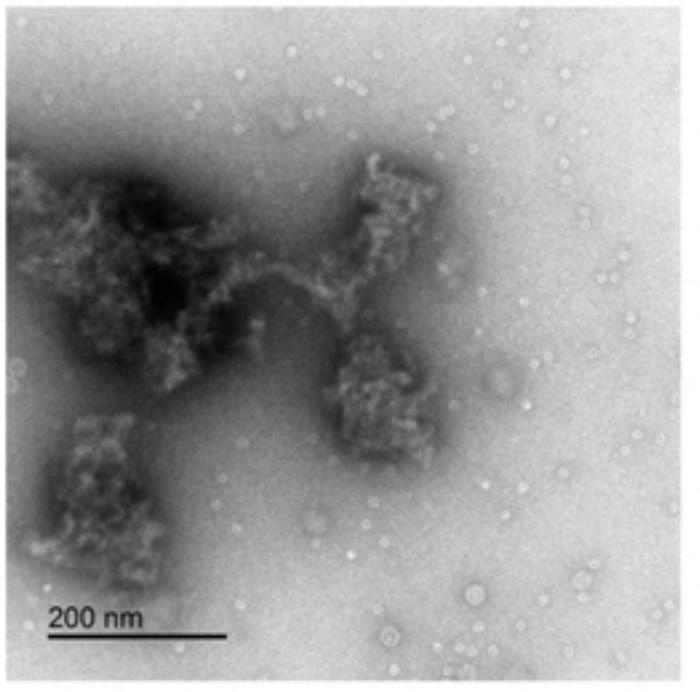

Fig2

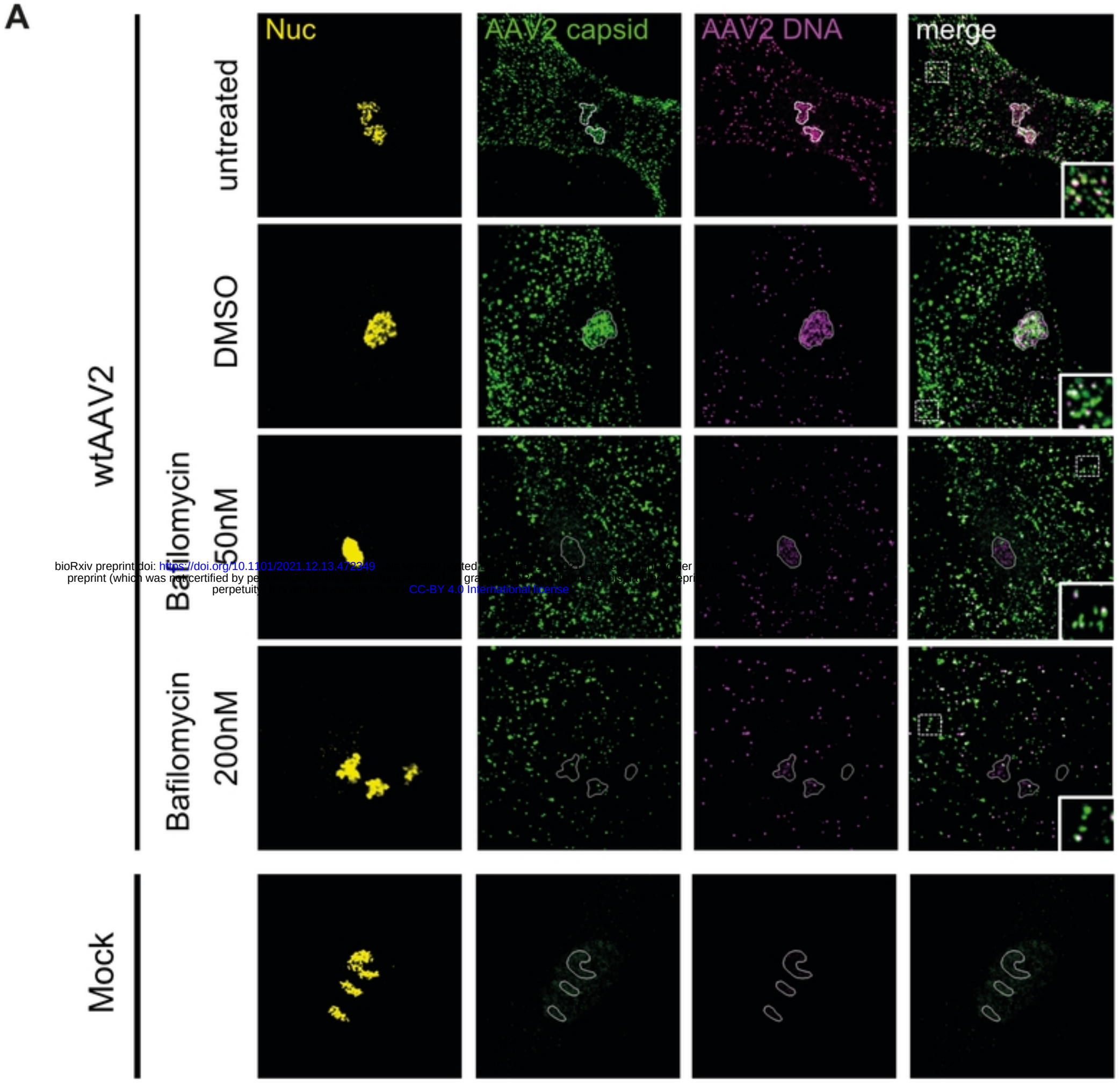

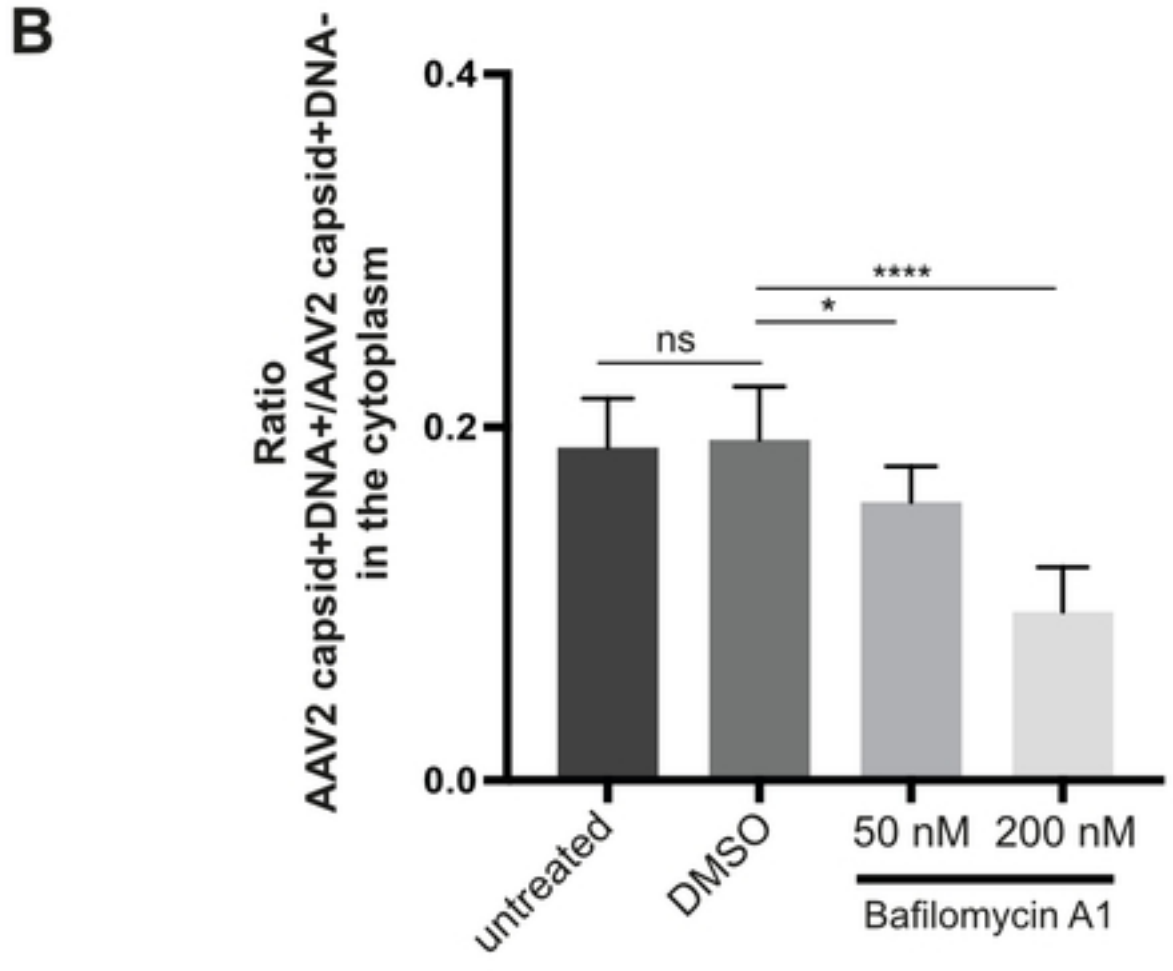

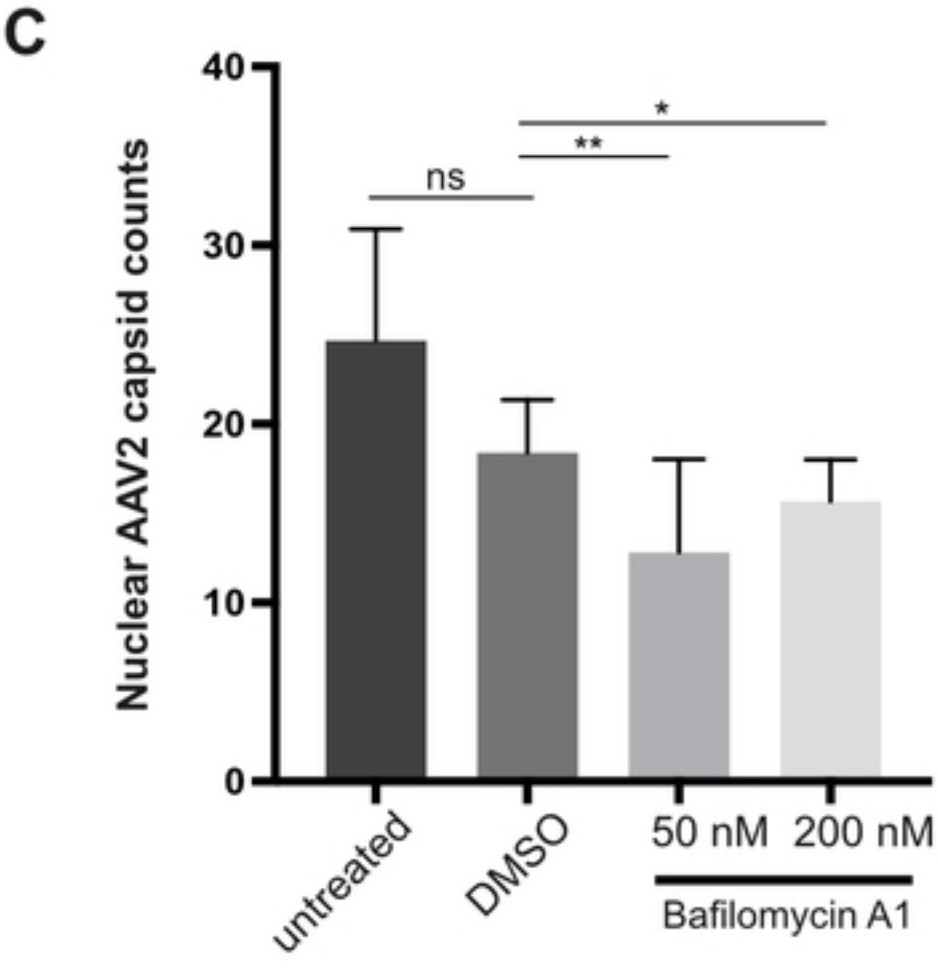

Fig3

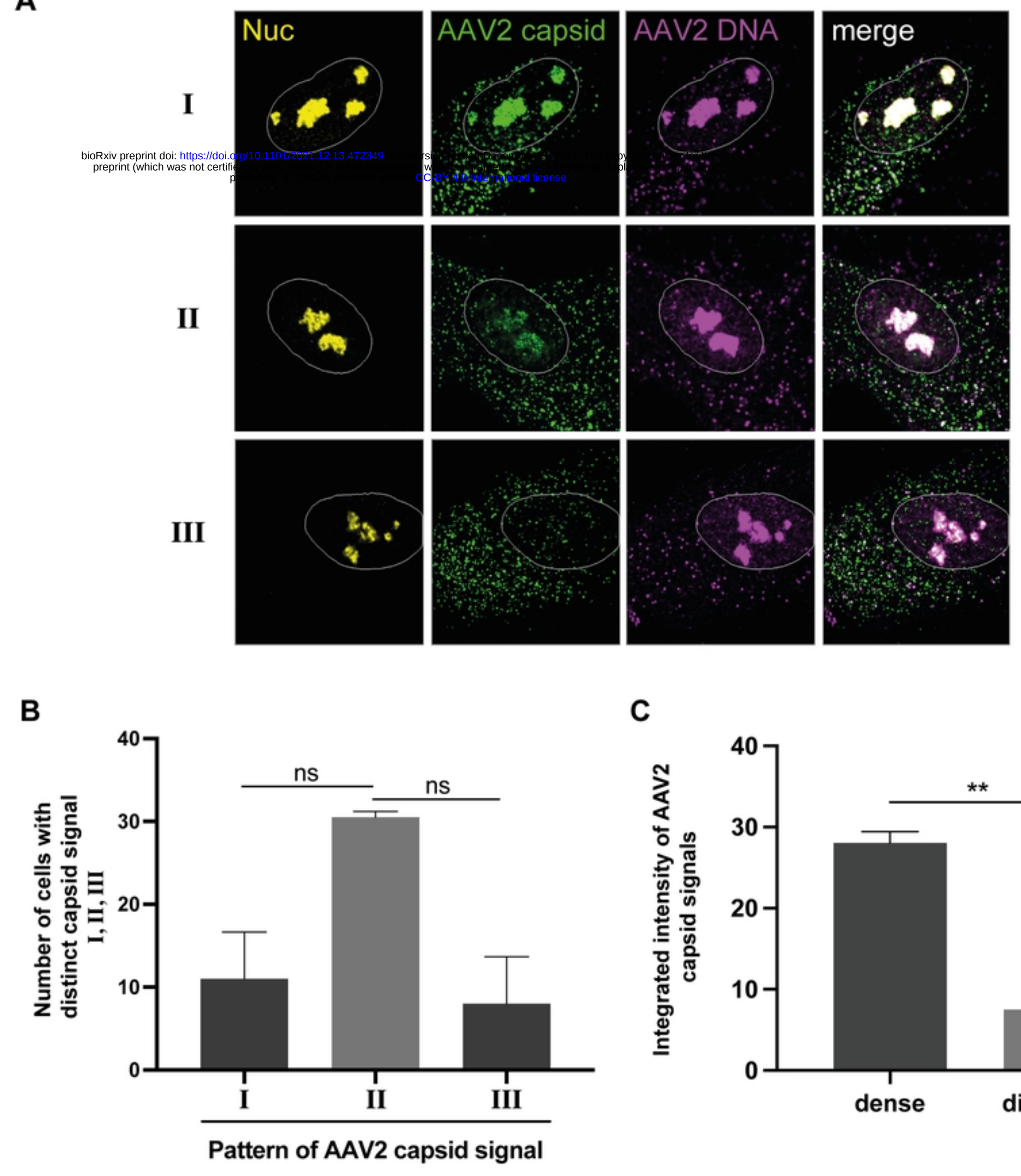

Fig4

A

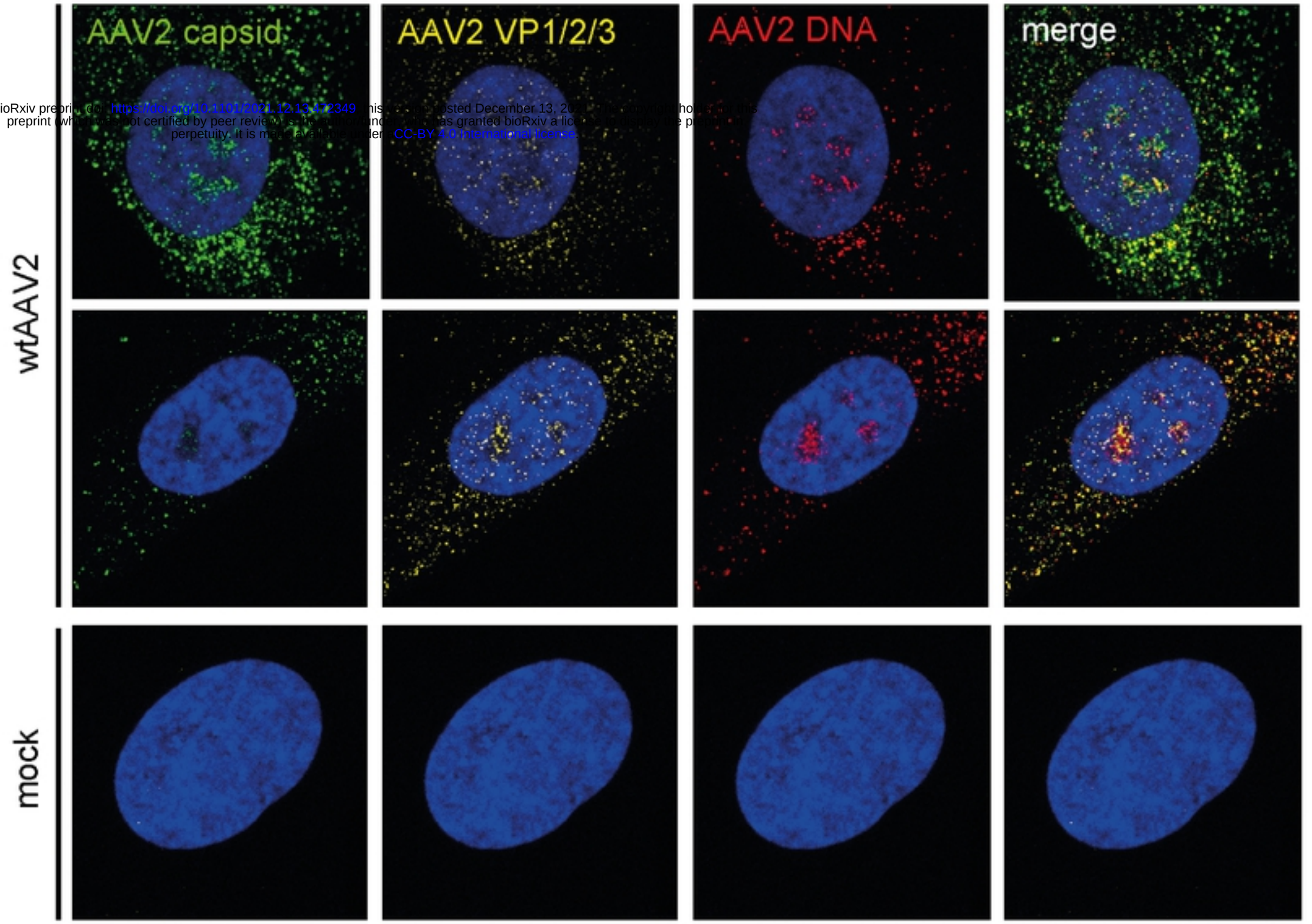

B

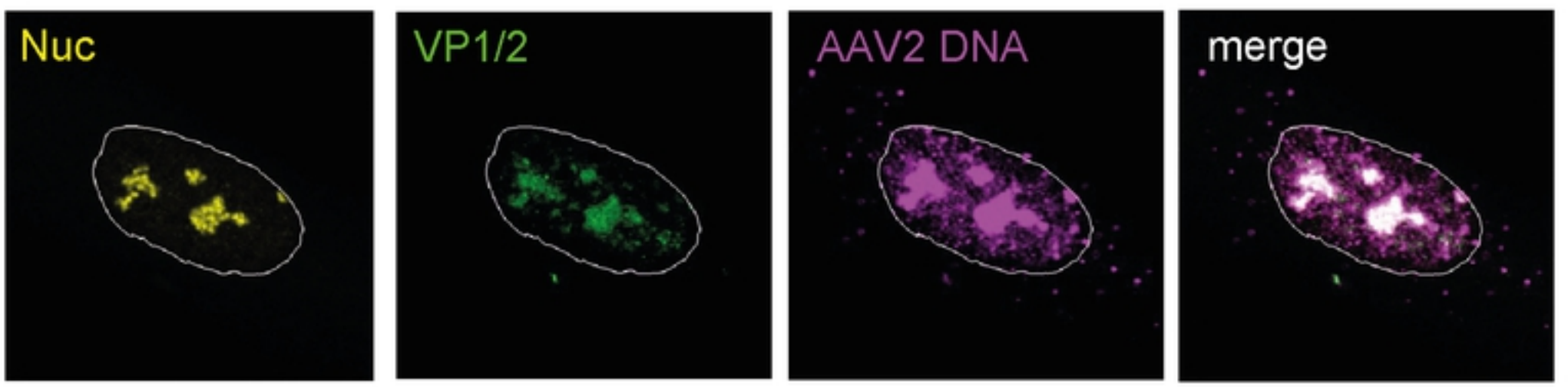

Fig5

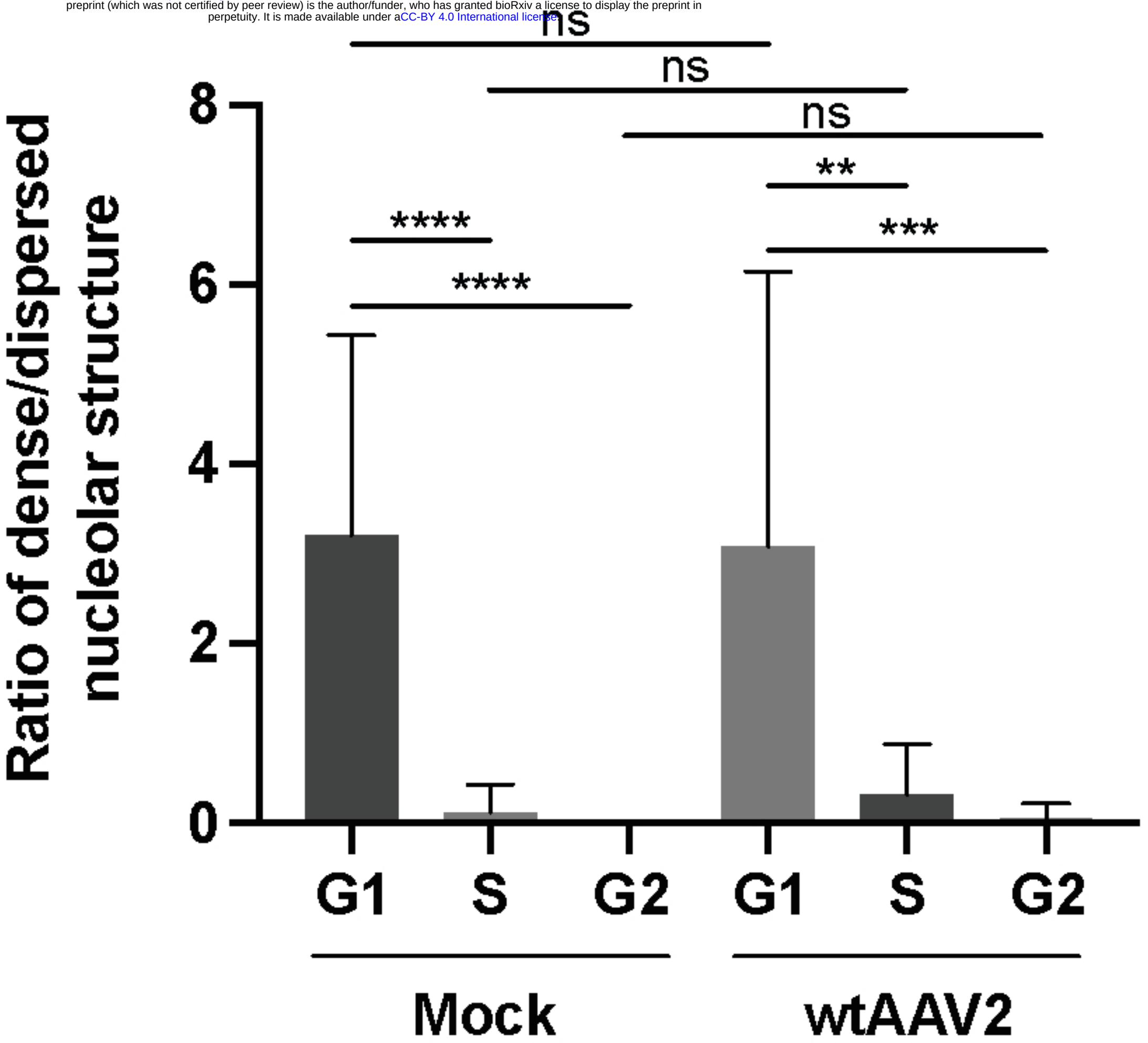

Fig6

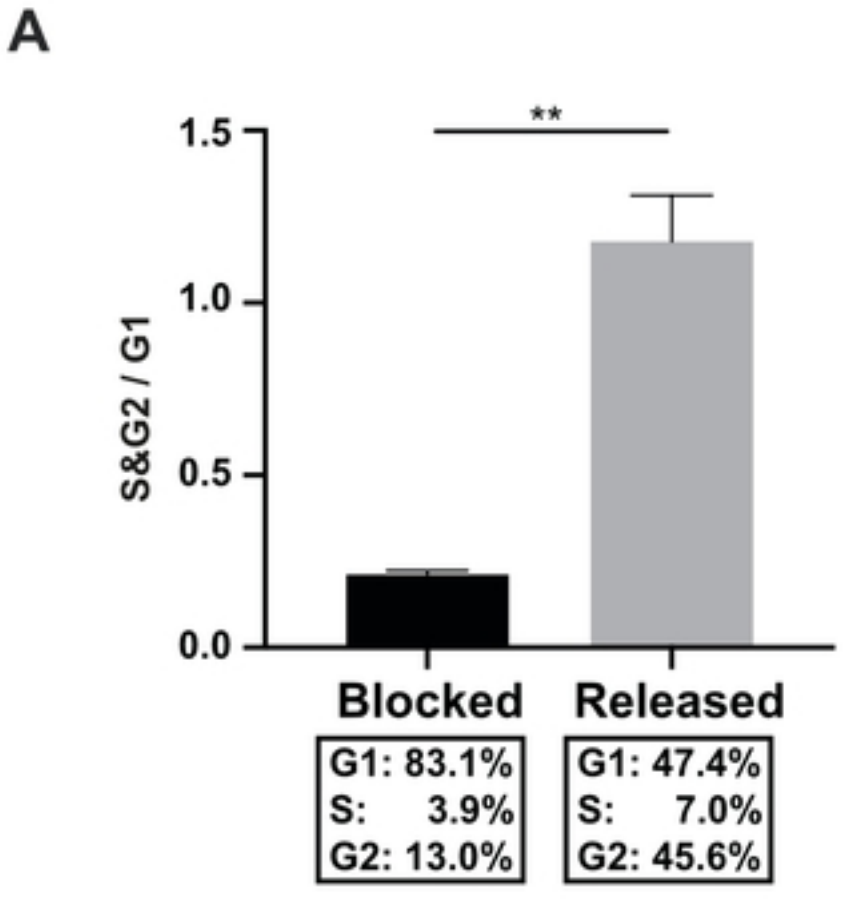
A
**
1.5
1.0
0.5
0.0
S&G2 / G1
Blocked
Released
G1: 83.1%
S: 3.9%
G2: 13.0%
G1: 47.4%
S: 7.0%
G2: 45.6%

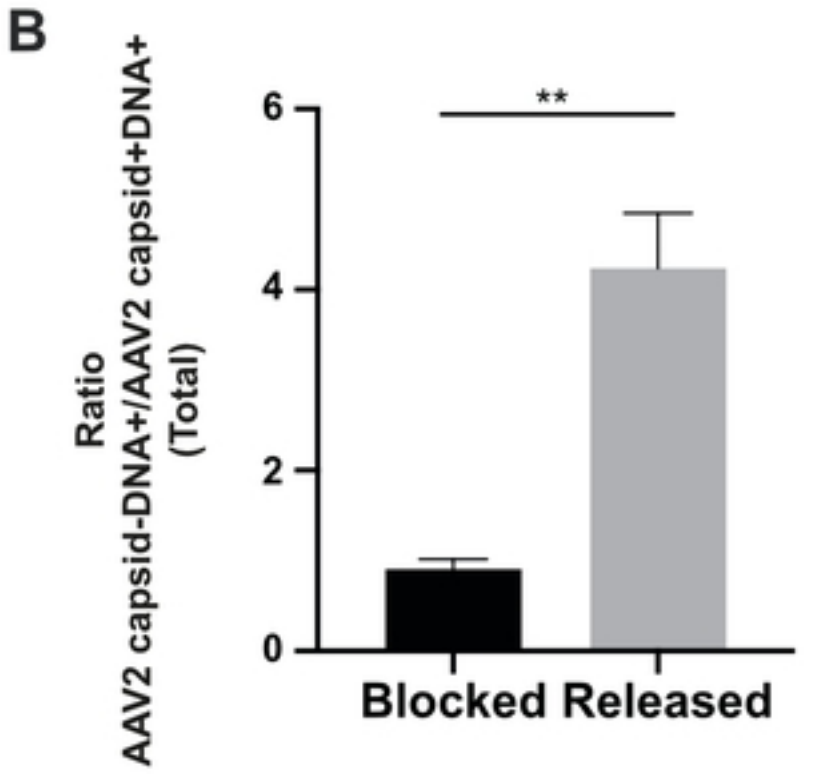
B
**
6
4
2
0
Ratio
AAV2 capsid-DNA+/AAV2 capsid+DNA+
(Total)
Blocked Released

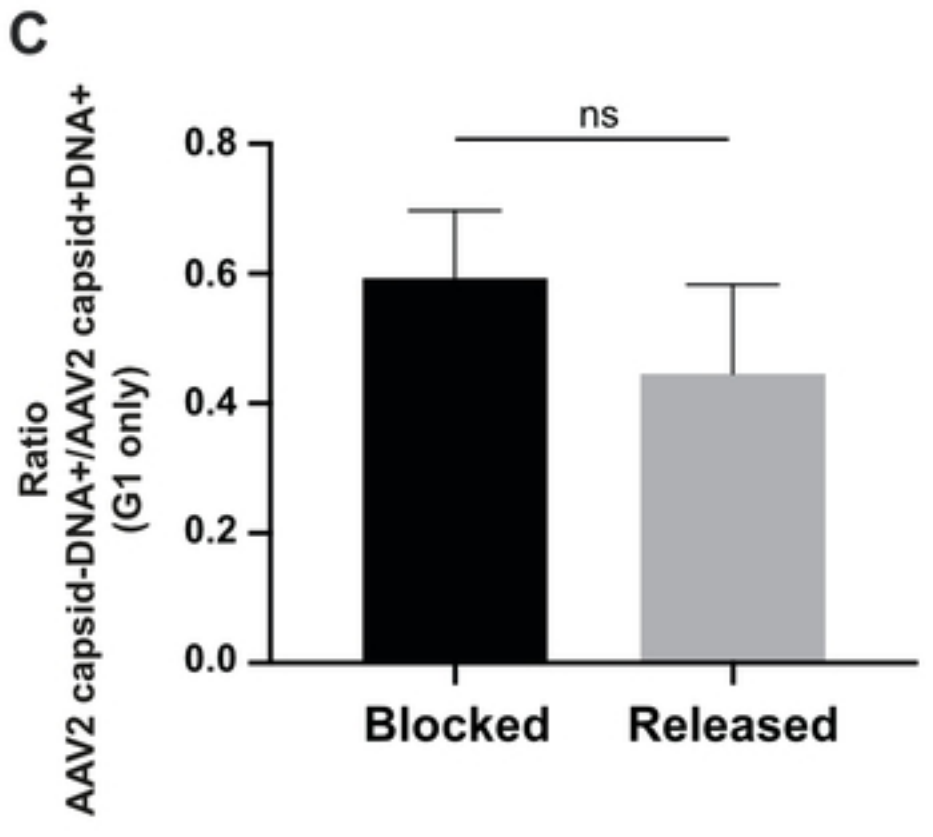
C
ns
0.8
0.6
0.4
0.2
0.0
Ratio
AAV2 capsid-DNA+/AAV2 capsid+DNA+
(G1 only)
Blocked
Released

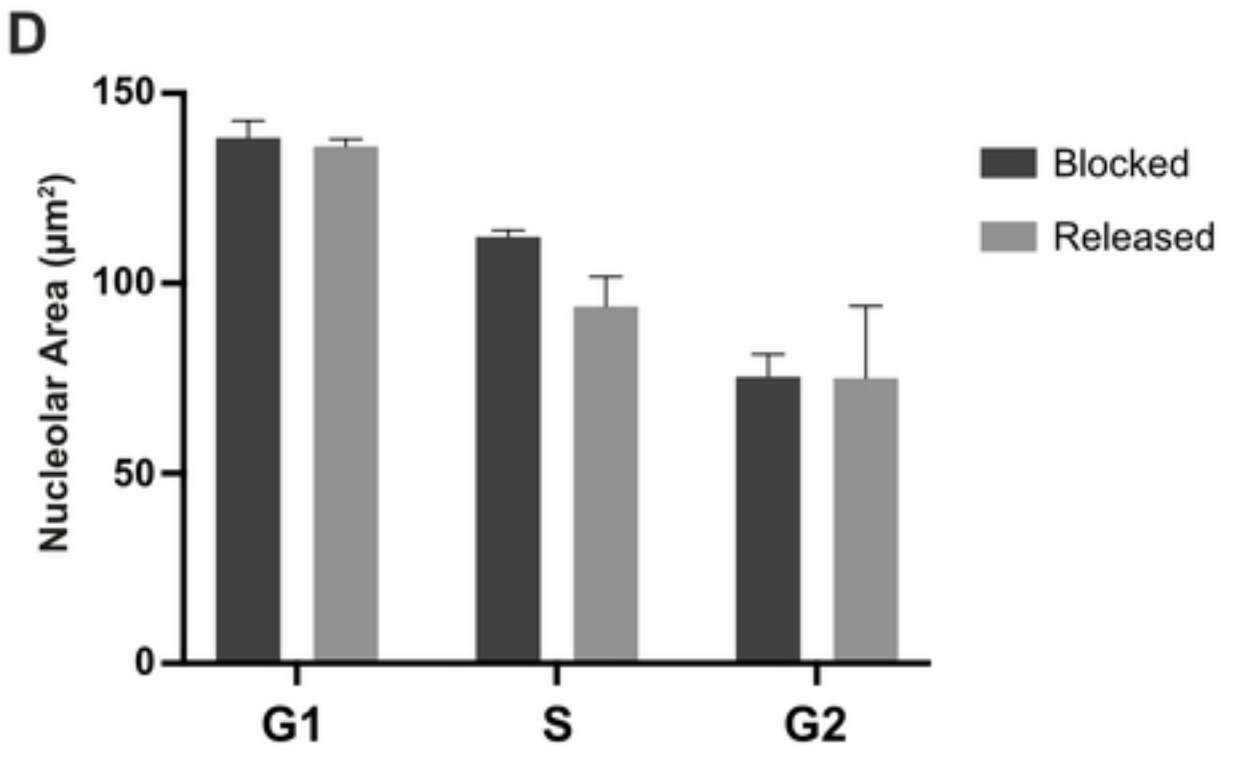
D
150
100
50
0
Nucleolar Area (μm²)
Blocked
Released
G1
S
G2

Fig7

A

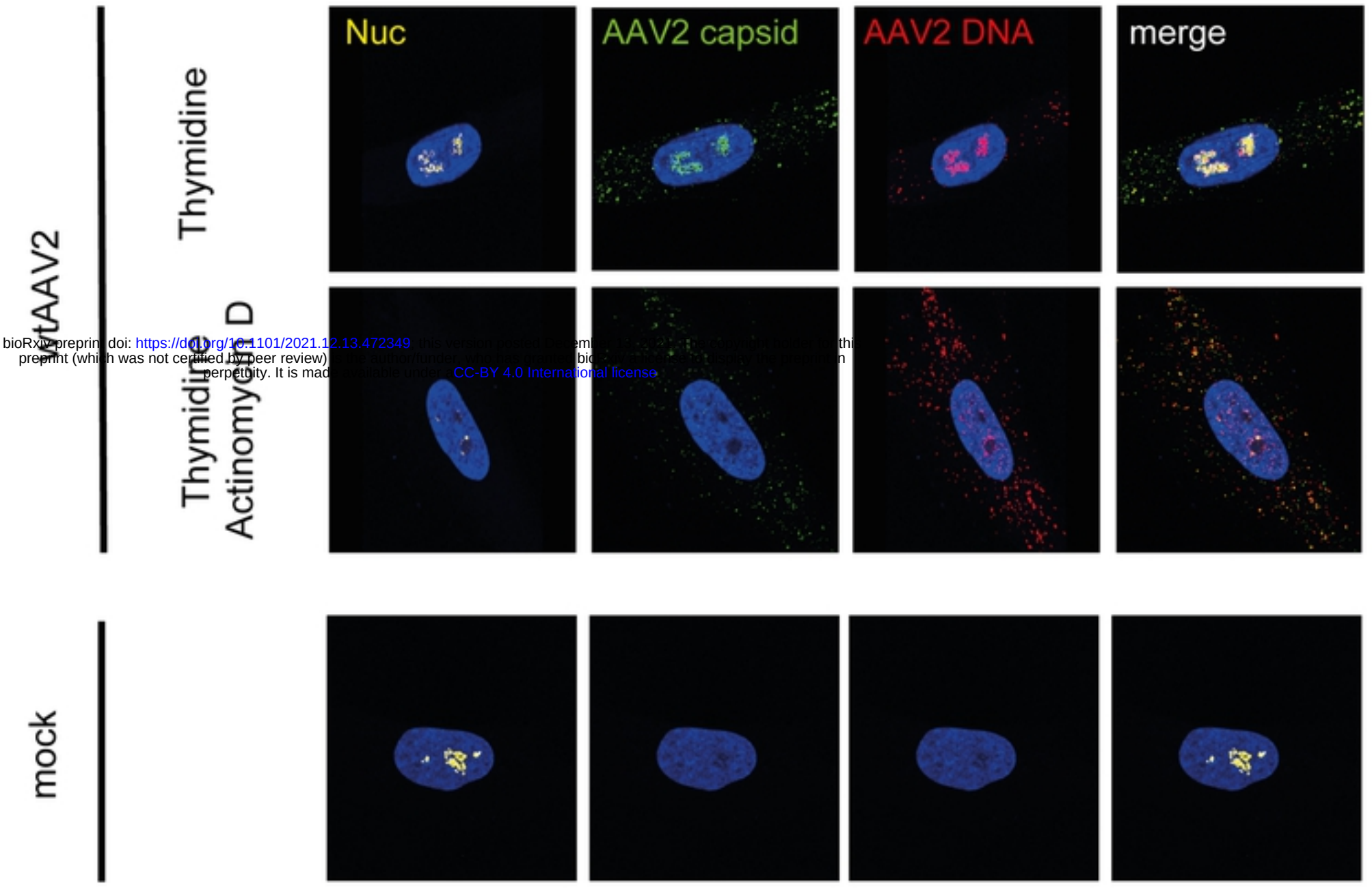

B

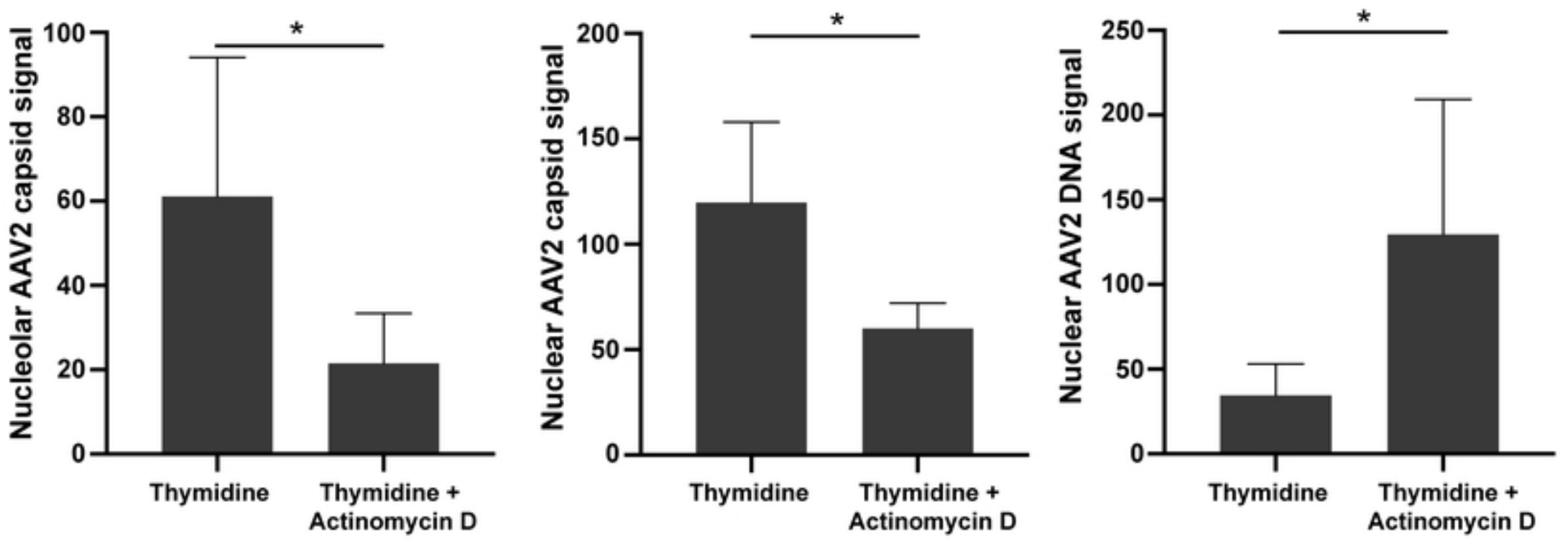

Fig8

A

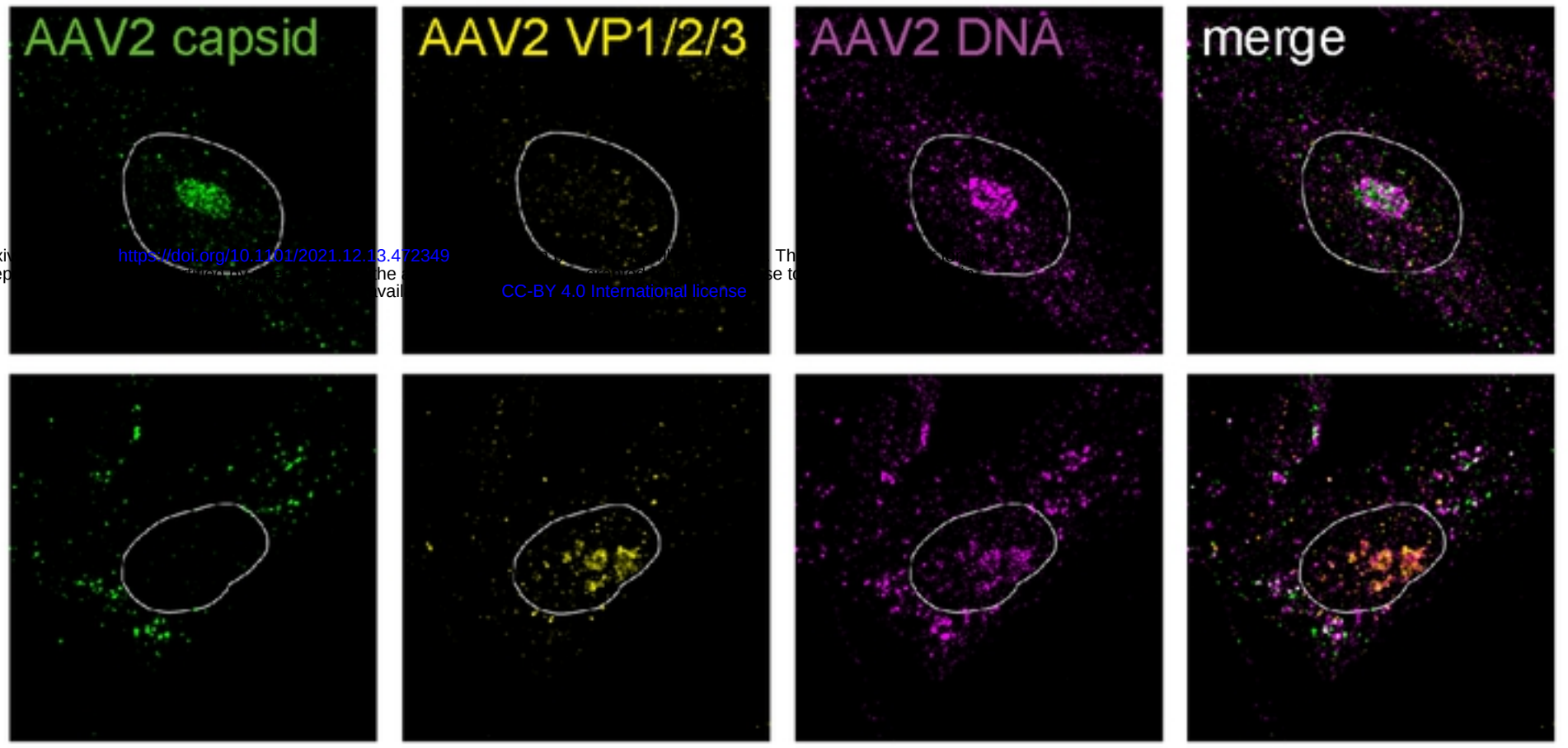

B

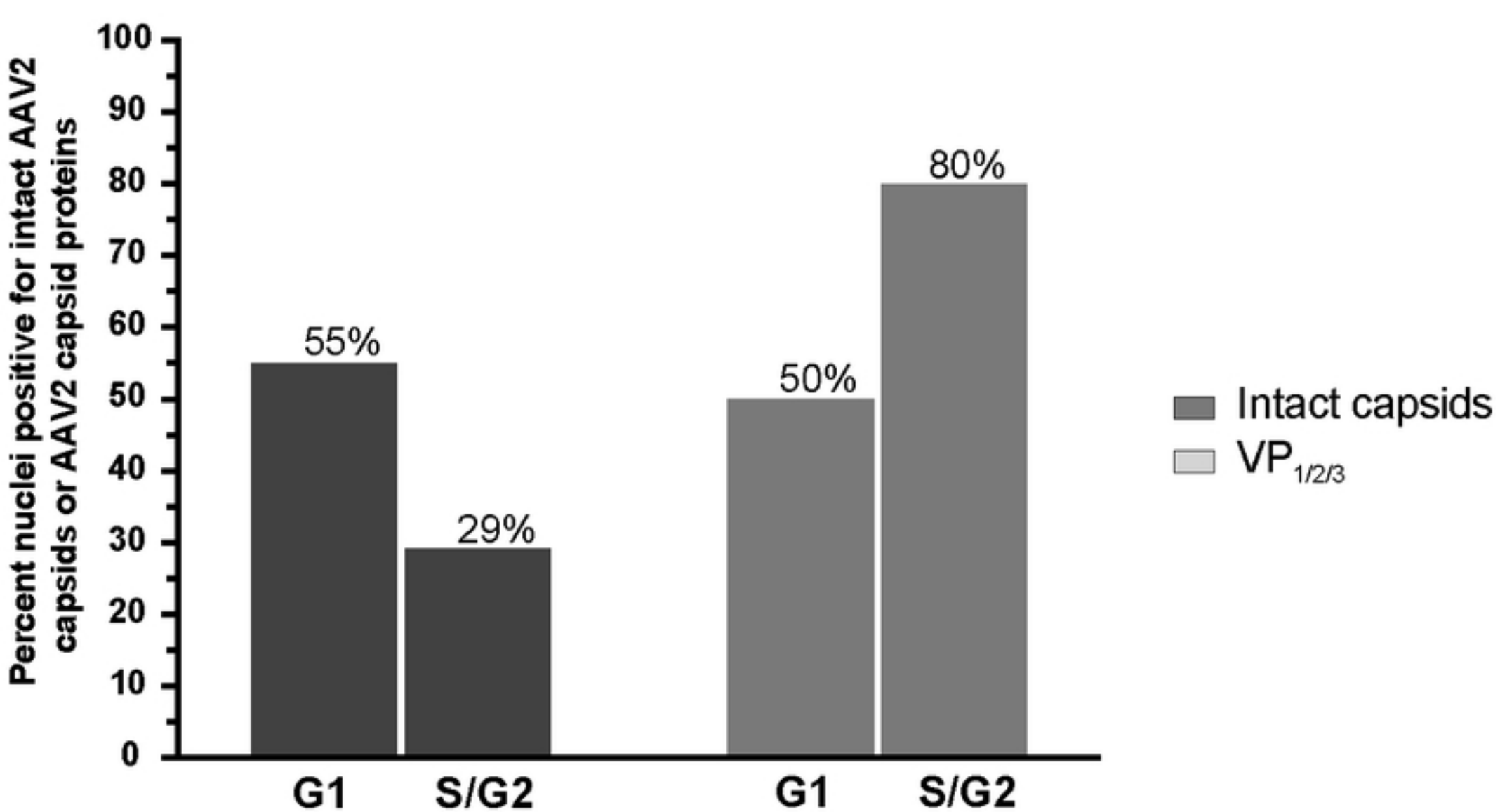

Fig9